Ocean Sci. Discuss., 9, 3795–3850, 2012
www.ocean-sci-discuss.net/9/3795/2012/
doi:10.5194/osd-9-3795-2012

Ocean Science Discussions

Daily scale winter-time sea surface temperature variability and the Iberian Poleward Current in the southern Bay of Biscay from 1981 to 2010

G. Esnaola[1], J. Sáenz[2], E. Zorita[3], A. Fontán[1], V. Valencia[1], and P. Lazure[4]

[1]AZTI-Tecnalia, Marine Research Division, Herrera Kaia Portualdea z/g, 20110 Pasaia, Gipuzkoa, Spain
[2]Department of Applied Physics II, Fac. of Science and Technology, University of the Basque Country (UPV/EHU), Barrio Sarriena s/n, 48940 Leioa, Spain
[3]Institute for Coastal Research, Helmholtz-Zentrum Geesthacht, Max-Planck-Straße 1, 21502 Geesthacht, Germany
[4]Department DYNECO, IFREMER, Centre de Brest, BP 70, 29280 Plouzané, France

Received: 15 November 2012 – Accepted: 5 December 2012 – Published: 18 December 2012

Correspondence to: G. Esnaola (gesnaola001@ikasle.ehu.es)

Published by Copernicus Publications on behalf of the European Geosciences Union.

Abstract

The combination of remotely sensed gappy sea surface temperature (SST) images with the missing data filling Data Interpolating EOFs (DINEOF) technique followed by a Principal Component Analysis of the reconstructed data, has been used to identify the time evolution and the daily scale variability of the winter-time surface signal of the Iberian Poleward Current (IPC) during the 1981–2010 period. An exhaustive comparison with the existing bibliography, and the vertical temperature and salinity profiles related to its extremes over the Bay of Biscay area, show that the obtained time series accurately reflect the variability of the IPC. A physical mechanism involving both atmospheric and oceanic variables is proposed in relation to the variability of the IPC. It jointly takes into account several mechanisms that have separately been related to the variability of the IPC, i.e. the south-westerly winds, the Joint Effect of Baroclinicity And Relief (JEBAR) effect, the topographic β effect and a weakened North Atlantic Gyre. This mechanism emerges from an atmospheric 500 hPa circulation anomaly that has not a simple relationship with any of the most common North Atlantic teleconnection patterns. It then generates mutually coherent SST and sea level anomaly patterns in the North Atlantic area due to the action of anomalous wind-stress and heat-fluxes, and locally, it also generates the conditions for the mentioned mechanisms in the Bay of Biscay area.

1 Introduction

The Bay of Biscay is located in the intergyre zone of the North Atlantic, between the Azores current in the northern part of the subtropical gyre and the North Atlantic current in the subpolar gyre. The general circulation in the intergyre area is slack, especially in the Bay of Biscay. Here, the water circulation is characterised by a weak anticyclonic flow in the oceanic area, a poleward slope current, slope water oceanic eddies, coastal upwelling in the western Iberian Peninsula, tidal flows, wind-induced

OSD
9, 3795–3850, 2012

currents and buoyant plumes (Koutsikopoulos and LeCann, 1996). In particular, the slope current is characterised by its baroclinicity, generating eddies, fronts, meanders, instabilities and other related processes (Pingree and Le Cann, 1990; Coelho et al., 1999; Gil, 2003; Peliz et al., 2005, among others). Therefore, a complex overall pattern of processes is established in the continental slope of the bay.

The poleward flow along the western Iberian margin was first reported by Frouin et al. (1990) and Haynes and Barton (1990), by using sea surface temperature (SST) satellite imagery and in situ measurements. The Iberian Poleward current (IPC) (Navidad current for late December to early January episodes) enters the Bay of Biscay around Cape Finisterre (NW Spain). Next, the warm and salty water flows eastward along the Cantabrian continental slope. Some flow continues poleward across the Armorican and Celtic slopes (Pingree and Le Cann, 1989, 1990). Since it is hindered by the abrupt changes of topography in locations such as canyons, the slope water is injected seaward to form slope water oceanic eddies (Garcia-Soto et al., 2002), the so-called SWODDIES (Pingree and Le Cann, 1992b).

The main forcing mechanisms of the IPC have been summarised by Coelho et al. (1999). The main mechanism for the generation of momentum has been attributed to the interaction of the meridional density gradient with the slope (Frouin et al., 1990). This is due to the geostrophic adjustment of the cross-shore density gradient that occurs when the large-scale eastward flow interacts with the slope of the N–S oriented coast (Relvas et al., 2007). This effect, the so-called JEBAR (Joint Effect of Baroclinicity And Relief), was theoretically described by Huthnance (1984). Frouin et al. (1990) also postulated that the prevailing winter west-southwesterly wind stress forcing generates only one fifth of the total poleward transport and considered the thermohaline forcing as the main driving process. Another forcing mechanism is the wind stress curl and its related poleward Sverdrup transport (Haynes and Barton, 1990; Le Cann and Serpette, 2009). Torres et al. (2003) concluded that the large-scale meridional density gradient is the main driving mechanism and that interannual IPC variability may be influenced by anomalous winds.

OSD
9, 3795–3850, 2012

Pingree and Le Cann (1990) noted that, although the mean slope current is relatively weak (5–10 cm s^{-1}), it is markedly seasonal with warm surface water flowing along the Portuguese and the northern Spanish slopes in winter. In summer, the fate of the poleward flow is still debated (Relvas et al., 2007). Pingree (1993) noted that surface flow in the northwestern Spain is significantly seasonal as indicated by seasonal changes in mean wind stress. Between February to October, the Azores High intensifies and the pressure gradient around the high also increases. This implies southward winds off the Portuguese coast, winds that cause upwelling and southward directed surface flows, particularly in summer. In winter, when the Azores High weakens, the southward component of the wind stress relaxes or even changes sign, allowing the extension of a surface warm poleward current. Therefore, there is a reversal of surface flow off the Portuguese slopes between summer (southward flow) and winter (poleward flow). Recently, Peliz et al. (2005) have proposed a seasonal cycle of development and decay of the poleward current in the Western Iberian Peninsula, based on previous studies (Frouin et al., 1990; Haynes and Barton, 1990). The phase of development implies the strengthening of the meridional density gradients during late autumn and winter within the Western Iberian Basin; the development of the IPC as a tongue-like structure as described in Frouin et al. (1990); and, the development of the turbulent character of the IPC. On the other hand, the decay phase is related to the weakening of the meridional density gradients in late winter; the broadening of the warm tongue and erosion of the near-surface thermohaline structure by the action of wind stress and interactions in the mesoscale eddy field; the offshore drift of the tongue and individual eddies (Peliz et al., 2005). The latter authors hypothesized that the poleward flow does not reverse but that the core is moved offshore.

The estimations of the interannual variability of the IPC have mostly been based on differences of SST between off-shore zones by the coast and open ocean areas (zonal or meridional differences depending on the location) (Pingree and Le Cann, 1992a; Peliz et al., 2005; deCastro et al., 2011) and also on collections of individual AVHRR SST images (Garcia-Soto et al., 2002; Garcia-Soto, 2004). An estimation

OSD
9, 3795–3850, 2012

of that variability that included the related salinity variability in addition to that of the temperature, was also given by Llope et al. (2006) based on in situ vertical temperature and salinity profiles. More recently, and based on a double variable approach, Le Hénaff et al. (2011) used a combination of two indexes to deduce a monthly winter IPC occurrence time series over the 1992–2002 period. The first index is based on Topex/Poseidon satellite single track (137) and it describes the geostrophic current anomaly. A second index is based on remote-sensed SST anomaly measured across the same satellite track. They found good agreement between the two indexes for the strongest 1995/1996 and 1997/1998 IPC episodes, but also some discrepancies, especially after 1999.

The relation of the interannual variability of the IPC with the North Atlantic Oscillation (NAO) index has been described in Garcia-Soto et al. (2002) and Garcia-Soto (2004). These authors found that January warming in the southern Bay of Biscay during exceptional IPC years was correlated with negative NAO index of the preceding months (November to December), indicating a relation between integrated effects of negative NAO phases from previous months on the ocean and the state of the IPC in January. The interannual variability of the SST in the area was also found to be anti-correlated with the preceding December NAO index over the 1965–2003 period by Michel et al. (2009), for all seasons in this case. Garcia-Soto and Pingree (2012) also found a link between the interannual SST variability in the Bay of Biscay and the Atlantic Multidecadal Oscillation (AMO) and pointed that the relative strength of the IPC occurrences could be related to this major climate mode. The state of the IPC in January was also found by Le Cann and Serpette (2009) and Le Hénaff et al. (2011) to be partly related to NAO index from preceding months. However, they concluded that the intensity of the IPC is not associated with the amplitude of the NAO index. Llope et al. (2006), in contrast, did not find a relationship with the NAO in their study based on temperature and salinity data. In addition to NAO, deCastro et al. (2011) also found relation with the November–December Eastern Atlantic Western Russia (EA/WR) teleconnection

OSD
9, 3795–3850, 2012

pattern. Pingree (2002) found similar anti-correlation between the NAO index and the poleward eastern boundary current at larger scale, from Portugal to Scotland.

Daily infra-red SST satellite products that cover more than the last three decades have shown to be a valuable tool for the detection of the surface signal of the IPC (Frouin et al., 1990; Haynes and Barton, 1990; Pingree and Le Cann, 1990, 1992a,b; Garcia-Soto et al., 2002; Garcia-Soto, 2004; Torres and Barton, 2006; Le Cann and Serpette, 2009, among others). In many cases, however, those images suffer from a high percentage of missing data, mostly due to the presence of clouds at the time they were remotely sensed. This fact has lead to the use of time averaged SST images or sparse exceptionally clear SST images in most studies related to the IPC. The first step of the present study will be to surpass the problem of the high percentages of missing data using the DINEOF technique to reconstruct as much as possible winter-time infra-red SST images. In addition, it will be tested whether it is reasonable to combine micro-wave and infrared remotely sensed SST images within the DINEOF technique as a way to enhance the number of reconstructed infra-red images. The rationale behind this idea is that the number of missing data in the micro-wave based dataset is much smaller. All deduced reconstructions will be validated using satellite-independent in situ data.

A Principal Component Analysis will then be applied to the reconstructed and validated SST images to identify the IPC signal on the SST. The first EOF and its time expansion series will be shown to properly characterize the IPC phenomenon by both the comparison with previous studies and the use of in situ temperature and salinity data. Once the IPC time evolution time series has been established, its extreme positive and negative values will be used to deduce the atmospheric and oceanic conditions related to such conditions.

Accordingly, the objectives of this study are the following ones. First, to obtain as much as possible missing data free winter-time SST images for the Bay of Biscay area applying the DINEOF reconstruction technique. The second objective consists in testing if the combined reconstruction of micro-wave and infra-red SST images leads to

OSD
9, 3795–3850, 2012

any improvement compared to reconstructing only infra-red images. The third objective tries to identify the IPC signal on the reconstructed datasets by deducing a daily frequency series of its occurrence for the winters in the 1981–2010 period, validating it based on satellite independent in situ data. Finally, the fourth objective consists in deducing the atmospheric and oceanic conditions that enhance or prevent the major IPC episodes. They are analysed within the context of the IPC driving mechanisms proposed in previous studies. The variety of used data sets and the DINEOF reconstruction technique are described in Sect. 2 and the results are presented in Sect. 3. Section 3.1 deals with the reconstructions of SST datasets and the validation of the reconstructed data, whilst Sect. 3.2 shows the deduction and validation of the IPC time series. Finally, Sect. 3.3 deals with the atmospheric and oceanic conditions related to the IPC. A discussion follows in Sect. 4 and the final conclusions are given in Sect. 5.

2 Data and methodology

2.1 Data

The variety of data sources used in this study is described in the following. First the satellite SST datasets to which the missing data reconstructing technique will be applied are described, followed by the description of the in situ measured SST dataset used for the verification of such reconstructions. Next, the reanalysis products used to study the influence of the atmosphere on the major SST variability modes are described. The properties of a satellite sea level anomaly (SLA) dataset used for the same purpose are also detailed. Finally, an in situ profile dataset used to obtain the vertical distributions of temperature and salinity related to the main SST variability pattern is described.

Two sources of remotely sensed night-time satellite sea surface temperature (SST) images covering the southern Bay of Biscay study area (Fig. 1) have been used in this study. One is based on measurements in the infra-red spectral band. The second is

OSD
9, 3795–3850, 2012

based on the micro-wave band. The differing characteristics of the two datasets and their relative advantages and disadvantages are summarised in the following, paying special attention to their spatial resolutions and time coverages.

The first source of SST images is the AVHRR Pathfinder V5.2 product (Casey et al., 2010) that offers nearly 30 complete years of 4 km resolution daily SST images retrieved from infra-red band radiometer measurements for the 1981–2010 period. The product also offers a full set of eight quality flags describing the reliability of each of the SST retrievals, going from 0 (lowest quality) to 7 (highest quality). Winter-time daily night-time quality flag 7 SST images were chosen for this study (ftp://ftp.nodc.noaa.gov). This choice strongly conditions the number of available SST retrievals but ensures the use of the best possible dataset in the application of the SST image reconstruction technique.

The second source of SST images is the v7 product derived from measurements by the Advanced Microwave Scanning Radiometer (AMSR-E) on board the Aqua satellite (http://www.ghcc.msfc.nasa.gov/AMSR/). With a 0.25° spatial resolution, daily images are available starting in June 2002. Files for the 2002–2010 period were obtained (ftp://ftp.ssmi.com) and processed to obtain winter (November-December-January-February) night-time daily images for the study area.

The Pathfinder SST image series, compared to these from AMSR-E, have the advantages of covering a longer period (1981–2010 compared to 2002–2010) and having a higher spatial resolution (4 km compared to 0.25°). However, these images, derived from measurements in the infra-red band also have a major disadvantage compared to the micro-wave retrievals since SST estimations are missing in the presence of clouds. Although AMSR-E images will contain missing values due to the occurrence of rain, strong winds ($> 20\,m\,s^{-1}$), sun glint or in areas near the coast (~ 75 km), the overall percentage of missing data is considerably smaller compared to the Pathfinder dataset. Despite their lower resolution and lack of measurements in locations near the coast, this property makes them a potentially valuable source of information to complement other higher resolution SST images with high percentages of missing data. Accordingly,

OSD
9, 3795–3850, 2012

instead of filling in missing values in AMSR-E data, the technical approach applied here is to use that available information in the reconstruction of missing Pathfinder data.

Once the reconstruction technique was applied to SST images and missing data was filled in, reconstructed SST fields have to be verified, preferably against independent data. In-situ SST measurements from the International Comprehensive Ocean-Atmosphere Data Set or ICOADS (Worley et al., 2005; Woodruff et al., 2011) were used for that purpose. Although observations from this source had already been used as an ensemble in the statistical procedure applied in the calibration of the algorithms used to retrieve SST from satellite measurements (Kilpatrick et al., 2001), and thus are not fully independent from satellite SST retrievals, individual in situ SST casts corresponding to the study area were used as a satellite independent source of information in the verification processes.

To check the oceanic vertical structure and the properties of water masses related to the main SST variability mode given by the PCA of the reconstructed Pathfinder SST data, vertical temperature and salinity profiles from the World Ocean Database (http://www.nodc.noaa.gov/OC5/WOD09/pr_wod09.html) were obtained for the study area, and subsets for the 5 different areas shown in Fig. 1 were selected. Winter-time profiles for standard depth levels corresponding to OSD, CTD and PFL instrumental sets (see Johnson et al., 2009, for details) and containing both temperature and salinity records were selected for the 1981–2010 period. Data for the 5 areas (I, II, III, IV and V) shown in Fig. 1 were separately analysed.

To study the covariability of the atmosphere and the winter-time SST in the area, atmospheric variables from the ERAInterim reanalysis (Simmons et al., 2007) were obtained for the North Atlantic area (55° W–11° E, 29° N–71° N). Night-time anomalies of the ERAInterim turbulent surface heat-fluxes ($W m^{-2}$), the surface pressure (hPa) and the two components of the surface wind stress ($N m^{-2}$), all with a 0.7° horizontal resolution, were obtained for the 1980–2011 period by removing the daily climatology. The surface turbulent heat fluxes, defined as positive when going into the ocean, are the sum of the surface latent and sensible heat fluxes.

OSD
9, 3795–3850, 2012

Additionally, 1.25° resolution daily anomalies of the geopotential height of the ERAInterim 500 hPa pressure level Z (m) were retrieved for the same period and area. The maximum values of the 3–10 day band-pass filtered intra-monthly standard deviations of such anomalies indicate the approximated location of the Northern Hemisphere storm track for each month (Lau, 1988; Rogers, 1997). In order to have a daily time evolution of that approximated location, 30-day moving standard deviations were used.

Daily scale sea surface gridded altimetry products were also obtained from AVISO (http://www.aviso.oceanobs.com) for the 1992–2010 period. The selected variables were the sea level anomaly (SLA) and the related geostrophic current anomalies, but the Absolute Dynamic Topography (ADT) was also obtained. The selected branch comprises delayed time data from different satellites (Topex/Poseidon, ERS-1/2, Jason-1, Envisat and OSTM/Jason-2) that are merged following a criteria for maximum temporal homogeneity ("Reference" data). A detailed description of this dataset can be found in AVISO (2012). The seasonal cycle was removed from both variables along with the long term trend.

2.2 Methodology

Initially described by Beckers and Rixen (2003) and Alvera-Azcárate et al. (2005), the Data Interpolating Empirical Orthogonal Functions technique (DINEOF) is an iterative methodology to fill in missing data in geophysical datasets. The technique initially sets missing values to zero value. Then the dataset is iteratively decomposed by means of a Principal Component Analysis (e.g. von Storch and Zwiers, 1999; Wilks, 2006) and recomposed afterwards using a fixed number of EOFs until convergence is achieved. The iterative process is repeated using a different number of EOFs in each realization. The optimal number of EOFs is determined by means of cross-validation using part of the initially non-missing data that is put aside for this purpose. Once the optimal number of EOFs is determined, a final reconstruction is conducted using all available non-missing data and the optimal number of EOFs previously identified.

OSD
9, 3795–3850, 2012

The methodology was additionally improved by Alvera-Azcárate et al. (2009) to reduce spurious time variability by including a filtering of the time covariance matrix that leads to better quality reconstructions. Examples of the application of the DINEOF technique can be found for the Adriatic Sea in Alvera-Azcárate et al. (2005), for the Ligurian Sea in Beckers et al. (2006), the Gulf of Mexico in Alvera-Azcárate et al. (2007) or the Black Sea in Alvera-Azcárate et al. (2009) among others. In the case of the Bay of Biscay and the surrounding areas, examples of DINEOF application can also be found in Sánchez et al. (2007), Ganzedo et al. (2011) or in Esnaola et al. (2012).

When applying the DINEOF technique to a dataset containing high percentages of missing data, it must be taken into account that the technique fills in missing values based on the available non-missing data. Frames (a time snap-shot) containing percentages of valuable information below a given threshold have to be disregarded, as their inclusion would worsen the overall skill of the reconstruction. A 5 % threshold of available non-missing data has been shown to be a reasonable choice (Alvera-Azcárate et al., 2005; Beckers et al., 2006) and was also used in this study. This means that only Pathfinder images belonging to days having non-missing data on at least a 5 % of the over ocean pixels were reconstructed. In case of the combined Pathfinder and AMSR-E reconstruction, days having a joint 5 % percentage of non-missing data were also reconstructed, leading to a higher number of reconstructed days compared to the reconstruction based solely on the Pathfinder data.

3 Results

3.1 Sea surface temperature reconstructions

The periods covered by the two satellite winter-time SST image sources, AVHRR Pathfinder V5.2 and AMSR-E, were 1981–2010 and 2002–2010, respectively. Based on that time coverage, two main DINEOF reconstructions and one supplementary reconstruction were carried out. DINEOF was first applied to the full Pathfinder data

OSD
9, 3795–3850, 2012

covering almost 30 yr. For the period shared by the two data sources, 2002–2010, a combined DINEOF reconstruction (Alvera-Azcárate et al., 2007) was then conducted, making use of the available AMSR-E data in the Pathfinder-based reconstruction. Finally, in order to have a mean to evaluate the impact of the inclusion of the AMSR-E data in the combined reconstruction over 2002–2010 period, DINEOF was additionally applied solely to the the Pathfinder over the same period.

It was previously stated in the methodology section that only SST images with less than 95 % of missing data were reconstructed. That means that only days with at least 5 % of available data were reconstructed for the two Pathfinder subsets (at least 5 % of quality flag 7 data available). In the case of the combined Pathfinder and AMSR-E reconstruction, the days that did not match that criteria but that had a joint proportion of 5 % available data were also reconstructed. The overall percentage of missing data (lower than quality flag 7) in the Pathfinder data set in the study area in winter-time over 1981–2010 is 93.2 %, in the set over 2002–2010 is 92.6 % and finally in the AMSR-E data set is 57.1 %. The number of days in each of the reconstructions matching the 5 % percentage threshold are shown in the first row of Table 1 (days), together with the percentage they represent with respect to the total amount of days in the period (in brackets). These percentages show that for the winter-time period, even allowing a threshold as high as a 95 % of missing data, the percentage of days trespassing the criteria remains low. However, the combined case shows the advantage of increasing that amount by approximately 4 %. For all the reconstructions, the percentage of the overall variance contained in the original datasets that was explained by their reconstructed counterparts was above the 99 %.

The rest of the Table 1 shows the values of the verification indexes computed using the in situ SST measurements from the ICOADS dataset. Based on the date and geographic location of each individual ICOADS observation, a check for the presence of a non-missing value was performed in the nearest neighbor satellite pixel and a verification sub-sample of N pairs of coincident values created. For each of these sub-samples two verification indexes were then computed: the bias (BIAS) and the median absolute

OSD
9, 3795–3850, 2012

deviation (MAD), that is qualitatively similar to the root mean squared error (RMSE) but less sensitive to outliers (Wilks, 2006). For each of the reconstructions, two verification sub-samples were selected. The first compared the originally non-missing satellite values with the available ICOADS counterparts (SATELLITE). A second comparison was made between all coincidences of the reconstructed and the in situ datasets (DINEOF).

The BIAS and MAD values in the SATELLITE columns give the approximated expected background differences between the in situ measurements and the satellite retrievals. It can be seen that DINEOF introduces a small negative BIAS in the 0.12–0.14 °C range. The MAD values of the reconstructed datasets remain nearly unchanged with respect to the original satellite and in situ value differences. Consequently, the verification Table 1 lists that error indicators are only slightly modified by the application of the DINEOF technique on the satellite data. It also shows nearly identical values for the 2002–2010 Pathfinder combined and non-combined reconstructions, indicating that the inclusion of the microwave satellite data in the reconstruction does not worsen its quality, but it increases the number of reconstructed days from 418 to 460.

The results shown in Table 1 correspond to the reconstructions based on quality flag 7 Pathfinder database values. Three additional analogous reconstructions were also computed (not shown) jointly using Pathfinder quality 5, 6 and 7 data. Due to the inclusion of new non-missing values, the percentages of reconstructed days increased, but this lead to an increase in the values of the error indicators, especially the BIAS. In view of these results, and to ensure the use of the best available SST images in the subsequent sections, only quality flag 7 data were subsequently used in spite of decreasing the number of reconstructed days.

In addition to the verification indexes given in Table 1, another two measures of the skill of the reconstructions are given in Figs. 2 and 3. First, in Fig. 2, as an indicator of the spatial distribution of the error introduced by the reconstruction technique, BIAS and MAD spatial maps obtained comparing originally non-missing satellite values with their reconstructed counterparts are shown (DINEOF technique was not required to

OSD
9, 3795–3850, 2012

retain the originally non-missing values unchanged). Figure 3 shows the time series of the BIAS and MAD values illustrating the time evolution of the errors, and also the number of observations used to deduce them. As in Table 1, the values obtained for the two combined and non-combined 2002–2010 reconstructions were very similar and thus only those belonging to the combined reconstruction are shown in both cases. Accordingly, both Figs. 2 and 3 are organized so that the first column shows the results of the 1981–2010 reconstruction and the second column those obtained in the 2002–2010 combined Pathfinder and AMSR-E reconstruction. Meanwhile, the first and second rows in Fig. 2 and the second and third rows in Fig. 3 show the BIAS and MAD results, and the first row in Fig. 3 the evolution of the number of observations used to deduce them.

BIAS values in Fig. 2 lay between ±0.25 °C range in most of the cases. Highest negative values are observed in the eastern corner of the Bay and positive ones in the western Iberian coast and also in the westernmost area in the case of the combined reconstruction. MAD values below 0.2 °C are more spatially homogeneous with highest values found in the western Iberian coast. However, no spatially remarkable pattern is found in the spatial error maps, which indicates that DINEOF does not introduce any specific spatial error signature with respect with the originally non-missing satellite values.

Considering again the comparison with in situ observations from ICOADS dataset, Fig. 3 shows the monthly time evolutions of parameters in Table 1. Again, the background error, i.e. the comparison of the originally non-missing satellite values and ICOADS observations (SATELLITE), and the errors of the reconstructions versus ICOADS observations (DINEOF) are shown (blue and red lines respectively). The time axes are arranged so that each space between the dashed vertical lines shows a November to February period (both included), and the same time axis is used for the 1981–2010 and 2002–2010 cases. BIAS values related to both reconstructions are mostly negative and lie between 0.2–0.4 °C values. However, there are important exceptions with considerably higher BIAS values in the case of the 1981–2010

OSD
9, 3795–3850, 2012

reconstruction, specially in the initial years, and also in some months in the 1992–1998 period. Although this could cause some concern on the quality of the reconstruction in these months, it has to be stressed that in almost all those cases with high BIAS values, the comparison of the originally non-missing satellite data and the in situ observations yields equally high BIAS values. This indicates that the error does not arise from the reconstruction itself but from prior discrepancies of satellite and in situ observations. The evolution of MAD values show a clear descending trend in the case of the Pathfinder alone reconstruction, and more constant levels with values in the 0.2–0.5 °C range for the combined 2002–2010 reconstruction. The decreasing trend in the 1981–2010 reconstruction seems to be related to both the increase of the number and the quality of in situ observations. In most cases, peaks with large MAD values in the SATELLITE original data are smoothed in the DINEOF reconstruction.

Table 1 and Figs. 2 and 3 show that the error estimations of the reconstructions based on the Pathfinder quality flag 7 data computed using the DINEOF technique are similar to the ones of the original raw data. These reconstructed data sets, however, offer a much larger amount of data compared to their original raw data analogues. These results support the use of the reconstructions in the forthcoming steps in this study. The main winter-time SST variability mode, and its relation with the Iberian Poleward Current and its variability, are studied in the following based on the reconstructed SST data.

3.2 Sea surface temperature variability and the surface signal of the IPC

The main winter-time SST variability mode, obtained from a PCA analysis of the reconstructed datasets, will be analysed in this section. In relation to this mode, the surface temperature pattern and the time evolution at different time scales, as well as the water mass properties related to them, will be shown to resemble well the properties inferred from several previous studies for Iberian Poleward Current. Due to its time span of nearly 30 winters, and the approximately 1250 SST images it contains, the analysis

OSD
9, 3795–3850, 2012

will be mainly based on the 1981–2010 Pathfinder reconstruction, but without totally discarding the combined 2002–2010 reconstruction.

The characteristic SST patterns related to a well developed IPC episode, and the presence of the surface signal of this phenomenon in the reconstructed datasets, is evident in the results from two selected previous studies based on gappy SST data which are reproduced here. These two examples will also be used to introduce the problem of identifying the IPC signal in SST anomaly patterns.

The SST anomaly maps were computed subtracting a 15-day running mean climatology from the individual daily SST images. Due to the recurrence properties of the IPC, part of its signal is present in the raw daily climatology, and accordingly the smoothing (15-day running mean) is an attempt to remove that presence. The presence of the IPC can be detected in the composed December–January mean of the daily smoothed SST climatology shown in Fig. 1, where a relatively warmer water intrusion can be detected off the northern Iberian coast. The image shows that even after such smoothing a weak IPC signal still remains in the daily climatology, and thus anomalies must be interpreted with care. It is also remarkable that the daily climatology shows the presence of colder waters near the western and north-western Iberian coast. This may have two origins. The first one comes from the upwelling events related to northerly winds. The second is the Western Iberian Bouyant Plume (WIBP) of riverine origin trapped by the coast by the effect of the IPC, described by Peliz et al. (2005). The detection of the IPC in the climatological mean could introduce some distortion in the interpretation of the anomalies. Although some drawbacks are related to the daily climatology used in this study, it will be shown that this climatology is consistent enough to characterize the IPC SST signal in terms of SST anomalies if the mentioned limitations are borne in mind.

deCastro et al. (2011) showed, using January mean SST maps computed from Pathfinder V5.0 data with missing values, years with and without evidence of the surface signal of the IPC (their Figs. 3 and 4). Here 1987, 1990, 1996 and 2005 Januaries were selected, the second and the third being months with evidence of IPC development and the other two without any clear evidence. Figure 4 shows 3 maps (columns)

OSD
9, 3795–3850, 2012

for each of these years (rows). The first column shows the mean January SSTs computed from Pathfinder v5.2 quality flag 7 gappy data and the second shows the same January means but computed from the reconstructed data. Figures from 1990 and 1996 yr effectively show the presence of 14–15 °C temperature surface waters near the western, and specially by the northern, Iberian coast, whereas their 1987 and 2005 analogues show equivalent 11.5–13 °C surface temperatures. The analogues of these results computed from the SST anomalies are given in the third column. Positive 0.5–1.5 °C anomalies are related to the presence of the surface IPC, both near and off the western and northern Iberian coasts, and are stronger in the north.

Figure 5 is related to two SST images that can be found in Le Cann and Serpette (2009) (Fig. 1b) and in Garcia-Soto and Pingree (2012) (Fig. 10b), but it also has the aim to illustrate the potential of the use of daily SST images. The figures in Le Cann and Serpette (2009) and Garcia-Soto and Pingree (2012) show a well developed IPC event on 14 December 2006. Figure 5 shows individual SST (first row) and SST anomaly (second row) maps for the 12, 14 and 16 of that month. The shape of the SST patterns is very similar to that shown in the mentioned references, including the meandering behavior off the continental slope related to the generation of swoodies (Pingree and Le Cann, 1992b; Garcia-Soto et al., 2002). The SST anomaly patterns are also consistent with the previous ones shown in Fig. 4. Additionally, Fig. 5 shows an intensification of the IPC signal, especially clear in the SST anomalies, over these five days. This result adds value to the reconstruction as such an intensification cannot be detected in the monthly averages used in previous studies. It is also very difficult to detect in the gappy SST images due to their high percentages of missing data.

Once the approximated shape of the IPC surface signal in SST anomalies has been introduced, the main winter-time SST variability mode and its relation with the IPC will be analysed. The determination of that mode will be based on a PCA of the SST anomalies. The results of such an analysis are very dependent upon the precise selection of the area. After checking different options (not shown), the best option for the purpose of capturing the IPC variability was found to be the area constrained between

OSD
9, 3795–3850, 2012

the 2000 m isobath and the coast. This choice is also supported by both the shape of the anomaly patterns in Figs. 4 and 5 and by the fact that as the IPC is a slope and shelf current, and consequently its surface signal is expected to be mainly located in that area.

The first Empirical Orthogonal Function (EOF) obtained from the reconstructed Pathfinder 1981–2010 SST anomalies is shown in Fig. 6. The equivalent EOF of the 2002–2010 combined reconstruction was nearly identical and thus is not shown (coherence of both EOFs was nearly 1). The EOF pattern explains a 49 % of the variance of the SST and it consists on a positive anomaly with values mainly in the 0.6–0.9 °C range. It is strongest in the western Iberian coast; to the north and east it follows the 1000 m isobath as the coast changes its orientation, then east of 7° W it follows the 200 m isobath as it weakens and finally it is reinforced in the corner of the Bay and to the North in the French coast. The standardized Principal Component (PC), i.e. the time expansion series, related to the first EOF, is shown in Fig. 7. As in the case of Fig. 3 only winter-time months are shown and February to November switches are identified by vertical dashed lines. Red dots show the 1981–2010 first PC and the blue dots the 2002–2010 first PC.

The spatial shape of the EOF is consistent with the surface SST anomaly patterns being related to a well developed IPC event previously shown in Figs. 4 and 5. Assuming that the EOF is at least partially related to a well developed IPC in terms of surface temperature signal, then the corresponding PC would be giving the approximate time evolution of the surface signal of the IPC during the winters over almost three decades. If strong enough evidence is collected to confirm such relation, the time series shown in Fig. 7 would be the longest estimation of the time evolution of the surface signal of the IPC. It would also be the estimation having the highest sampling frequency. To test that hypothesis, the reconstruction of the IPC occurrences will be described within the context of previous studies. Then, based on the WOD profiles, additional evidence will be given by means of the vertical structure and water mass properties related to the strongest occurrences and non-occurrences of the IPC in that series.

OSD
9, 3795–3850, 2012

The IPC has been usually detected in the past in infra-red satellite images. Along with these images in situ cruise and station measurements (temperature, salinity, currents, ...) and, later, satellite altimetry and related products have also gained increasing relevance. Some estimations of the winter IPC interannual variability on the yearly and monthly scales have also been derived based on that data. Table 2 summarises the documented detections of the IPC during the last decades showing the dates, the employed techniques and references of different studies. Based on the comparisons of these results, the hypothesis that the time series displayed in Fig. 7 represents the surface signal of the IPC will be checked in the following paragraphs.

All the detections based on individual SST images in Frouin et al. (1990), Haynes and Barton (1990), Pingree and Le Cann (1990, 1992a,b), Garcia-Soto (2004), Torres and Barton (2006) and Le Cann and Serpette (2009) are confirmed by our IPC signal estimation. For the case of the images shown or referenced by Garcia-Soto et al. (2002) most of the occurrences and non-occurrences are confirmed with the exceptions of January 1986, 1991, 1992 and 1994, when weak events are described by those authors. January 1999 is described as a non occurrence year by Garcia-Soto et al. (2002), but the early development phase of the IPC was reported near the west and north-western Iberian coasts for late October and the beginning of November of that year by Torres and Barton (2006). Our estimation indicates that two or three alternating positive and negative phases occurred, the first one possibly indicating the developed phase of the onset described by Torres and Barton (2006). However, 1999 stands out among the noisiest years in our series. The comparison with the images given in Garcia-Soto and Pingree (2012) also shows a high level of coherence, as all the occurrences are confirmed with the only exception of 2001 (see Table 2), when our estimation yields an approximately null value. The SST images in Herbert et al. (2011) showing the clearest IPC signal evidence for the end of January and the beginning of February 2004 are confirmed by our series but this is not the case for the rest of the figures, where the signal is not very clear. The result is similar to that obtained for the comparison with individual images from Le Hénaff et al. (2011), where clearest 1993,

OSD
9, 3795–3850, 2012

1996 and 1998 cases are confirmed. The signal is not very clear for the case of the 2001 January (the number of reconstructed days in that month is small). The January 1997 case shown by the authors shows an IPC-like signal in the current anomalies but it is not the case for the corresponding SST image, and does not find confirmation in our series. In the case of SST images used in studies only focused on the western Iberian coast (Peliz et al., 2003, 2005) both agreements and disagreements can be found, which is not surprising as the shape of the EOF in Fig. 6 indicates that the series in Fig. 7 would represent well developed IPC episodes (i.e. entering the Bay of Biscay). For the case of the estimations based on in situ cruise and station measurements, a good agreement is found for Torres and Barton (2006) and Le Cann and Serpette (2009).

Concerning the estimations of the interannual variability of the IPC, the very first estimation was obtained by Pingree and Le Cann (1992a) for the 1984–1991 period (3 values per winter). Taking into account that the anomalies from their series were relative to the 1985 values, and considering accordingly the anomalies from our series with respect to the 1985 values, a good agreement is observed between both series. Yearly series given in Peliz et al. (2005) and deCastro et al. (2011) are methodologically similar as both are based on the zonal SST gradient off the western Iberian coast, but for different months: the first one for December–January means and the second one only for Januaries. A general good agreement is obtained for both series, except for 1997 and 1999 in Peliz et al. (2005) and 1991 and 1995 in deCastro et al. (2011). Comparing together the series from those two studies with our series, it appears that the year 1999 shows the most remarkable differences, although other smaller differences also occur, both with our series but also among these two series themselves. Based on January images, Garcia-Soto et al. (2002) and Garcia-Soto (2004) make a classification of IPC (Navidad) and non-IPC years in the 1979–2004 period. For the January IPC events described by these authors, only the one in January 2001 in our series seems to disagree. However, the number of reconstructed days is very limited in that year. With respect to the relative strength of the IPC episodes over 1979–2004

OSD
9, 3795–3850, 2012

period, year transitions from 1989/1990, 1995/1996, 1997/1998 and 2002/2003 are considered the strongest by these authors. All of them are among the strongest in our series. However these author's January-centred description lacks other strong events that occurred earlier in November–December of that period, like those from 1983/1984, 1988/1989 or 1994/1995. In the case of the series of the vertical T/S profile estimated by Llope et al. (2006), the level of agreement with temperature profiles is acceptable for most of the years, although the comparison is not clear for 1998/1999 and 1999/2000 and a disagreement is detected for 2002/2003. The already considered Garcia-Soto (2004) and Llope et al. (2006) estimations are the basis of the estimation given by Le Cann and Serpette (2009), so no further comparison is needed in this case. Finally, the comparison with the IPC occurrence series of Le Hénaff et al. (2011), i.e. the monthly SST and geostrophic current anomaly indices, shows that the two main episodes in 1995/1996 and 1997/1998 described by these authors are consistent with our estimations for these years. For the rest of the years the agreement level is uneven, especially with the current anomaly index.

In the following, additional confirmation of the validity of our IPC series will be obtained based on the combination of its extremal properties and the WOD data. The two dashed horizontal lines in Fig. 7 show the 80th and 20th percentiles of the 1981–2010 PC series. Days in the time series above the 80th percentile are those related to the best developed IPC events according to the PC and will be denoted P80. Meanwhile, those below the 20th percentile represent the periods without, or with very weak, poleward flow and will be denoted P20. The properties related to these two groups will be used as indicative of the conditions related to well developed IPC events and to their opposite conditions in terms of the PCA mode. For each set of days, P80 and P20, the available WOD vertical temperature and salinity profile data were selected for each of the 5 area boxes (I, II, III, IV, V) and the corresponding temperature and salinity means were computed for each depth. As Torres and Barton (2006) found, the major poleward signal off the slope, characterized by the 200 m isobath, only vertical profiles located off the slope will be considered. To include a larger number of profiles for each case,

OSD
9, 3795–3850, 2012

and as the time scale related to the onset of poleward flowing surface warm anomalies has been estimated to be around a 5–10 day period (Torres and Barton, 2006), the P80 and P20 day sets were expanded adding the previous and subsequent 5 days to each date in the sets. Figure 8 shows the mean vertical temperature and salinity profiles denoted P80-Temp (solid red), P20-Temp (dashed red), P80-Salt (solid blue) and P20-Salt (dashed blue). For depths where the temperature (salinity) means P80-Temp (P80-Salt) and P20-Temp (P20-Salt) reject the null hypothesis that they belong to the same sample mean by more than a 95 % confidence given by a *t*-test (Wilks, 2006) a dot is added in the profile. The number of individual profiles taken into account in each mean is also shown by each corresponding label.

Vertical temperature profiles in the areas close to the Iberian coast (I, II, III) show the presence of significantly warmer waters in the first 100–200 m for the P80 set of days compared to those of the P20 set. In the case of the P80 set, the surface temperature value is 16.4 °C for the I area and approximately a degree colder for areas II and III. Following the path of the poleward flow, the same progressive cooling is observed also for the P80 set for temperatures at 50 m (16.2 °C, 15.1 °C, 14.8 °C) and 100 m (14.7 °C, 13.6 °C, 13.3 °C) depths, with a 1.1 °C cooling from area I to area II and a 0.3 °C one from area II to area III. The salinity pattern is more complicated than the temperature in each area, especially because enhanced salinity values are observed for P20 in the area I, which is not the case for areas II and III. In the case of the P80 salinities, subsurface maxima are found for areas I and II at 75 m (> 35.95 psu) and 125 m (> 35.75 psu) depths respectively. The open ocean area IV was introduced to check whether any influence of the IPC could be detected there (entire coverage of area IV is detailed in the caption of Fig. 1). The vertical profiles of the open ocean area IV indicate no major difference between the P80 and P20 sets, meaning that the poleward flow is confined to areas near the slope. Finally, area V was introduced as water masses from this area are expected to flow to area I first and then northwards during active poleward flow episodes (Peliz et al., 2005). Vertical profiles from this area show small differences in the deeper levels but no significant ones in the upper levels. However, a very good

OSD
9, 3795–3850, 2012

agreement is observed between the P80 temperature and salinity profiles and those from the area I, confirming the eastward flow from area V to area I.

The Temperature/Salinity (T/S) characteristics of the layer from the surface to 500 m depth in the WOD data are shown in Fig. 9 for the same 5 areas, including also over-shelf (depth < 200 m) profiles. Temperature and salinity pairs belonging to the P80 and P20 sets are represented by red and blue circles, respectively, and by green and light blue triangles for over-platform values. The definition curves of the two varieties of the Eastern North Atlantic Water (ENAW) found in the area, the colder $ENAW_P$ (subpolar) and the warmer $ENAW_T$ (subtropical), are shown in the T/S diagrams (Ríos et al., 1992). The poleward flow signature (warmer red and green symbols) is most clearly seen in the area I, but is also evident in areas II and III. A modification of the water mass properties is observed following the IPC evolution path from area I to area III, with a progressive decrease in the proportion of $ENAW_T$. The eastward evolution of the T/S characteristics on the northern coast (area II to III) is also consistent with those found by Llope et al. (2006) and Le Cann and Serpette (2009). Llope et al. (2006) also show the transition from non-IPC to IPC conditions in terms of T/S relationships in October–November 1999, which is fairly consistent with the differences between the P80 and P20 cases shown here. The IPC related sub-surface salinity maximum is most clearly detected in the case of the area II. Some evidence of local water mass property modification in the corner of the Bay of Biscay can be detected for both the P20 and P80 sets (around 12.5 °C and 35.55 psu), but specially for the former. In the case of of the area IV similar results are obtained for both sets, with a possible salinification for the P20 set. No water mass of $ENAW_T$ origin seem to reach this area in any of the cases. Finally, the area V shows an enhanced proportion $ENAW_T$ for the P80 as expected, and a diminished but still present portion of $ENAW_P$.

Through this section, an estimation of the time evolution of well developed IPC events, as well as the related SST structure, were obtained in terms of the first variability mode of a PCA analysis of the reconstructed SST. The validity of the time evolution series was then checked by comparison with all estimations that were available up

OSD
9, 3795–3850, 2012

to now and a good correspondence in most of the cases could be found. In addition, further confirmation of that validity was obtained based on vertical temperature and salinity distributions and T/S. In the following, the estimated and validated time series will be used to analyse the mechanisms that control the variability of the surface signal of the IPC.

3.3 Insights on the Iberian Poleward Current variability mechanisms

Previous studies on the interannual variability of the IPC have mainly focused on the NAO teleconnection pattern (i.e. Garcia-Soto et al., 2002; Garcia-Soto, 2004; Llope et al., 2006; Le Cann and Serpette, 2009; Le Hénaff et al., 2011), although some evidence for the relation with the EA/WR (East Atlantic/West Russia) pattern has also been found (deCastro et al., 2011). All these studies describe lagged integrated relations, among which the relation of January IPC occurrences and the negative mean November–December NAO index is the most recurrent (IPC-J NAO-ND). The relations with the main monthly Northern Hemisphere teleconnection were studied here as well. A monthly version of the daily frequency IPC time series (Fig. 7, grey bars) was used for that purpose. Standardized monthly series related to the NAO, Eastern Atlantic (EA), EA/WR, Polar/Eurasia (POL) and Scandinavia (SCA) teleconnection patterns were obtained from the Climate Prediction Center (CPC at NCEP) (http://www.cpc.ncep.noaa.gov). Synchronous and lagged correlations were checked, allowing also time integrated combinations. The significance level for meaningful correlations was set at 99 % (estimated by a Monte Carlo test).

Nine significant correlations were found (22 for the 95 % confidence level) corresponding to NAO (5), EA (2) and EA/WR (1) and SCA (1): IPC-NDJF NAO-ONDJ (−0.29), IPC-NDJF NAO-SOND (−0.27), IPC-N NAO-ON (−0.57), IPC-D NAO-ON (−0.49), IPC-J NAO-ON (−0.49), IPC-NDJF EA-NDJF (0.28), IPC-D EA-D (0.51), IPC-J EA/WR-ND (0.48) and IPC-F SCA-F (−0.57). In the case of the NAO all five correlations found are negative, positive for EA and EA/WR and negative for SCA. This means that negative phase NAO and SCA patterns and positive phase EA and EA/WR have

OSD
9, 3795–3850, 2012

been found to be related to increased IPC occurrences, which seems reasonable in view of their corresponding spatial patterns (e.g. see Fig. 6 in Garcia-Soto and Pingree, 2012). Considering individual months, November IPC is found to be related to October–November NAO and December IPC with October–November NAO and December EA. In the case of January IPC, relationship is found with October–November NAO and November–December EA/WR; and finally, February IPC is found to be related to February SCA. It is also interesting to note that delayed relationships arise for NAO and EA/WR while synchronous correlations are detected for EA and SCA.

Garcia-Soto et al. (2002) and Garcia-Soto (2004) show a strong relation between the most marked January IPC occurrences and the preceding November–December NAO index. In Garcia-Soto and Pingree (2012) a relation of the Bay of Biscay SST with the AMO is also shown and a possible relation with the IPC is suggested. If only the months of January with the strongest IPC occurrences (above 80th percentile) are considered (6 in total) only the combination with November NAO yields a significant correlation (0.94). Meanwhile, none of the combinations with the AMO index yielded significant correlations (99 % level).

The above mentioned correlations indicate that the interannual variability of the IPC is characterized by a fairly complex group of relations that goes far beyond a relation with a single atmospheric teleconnection pattern and points to a more complex combination of atmospheric circulation anomalies. Using the extremal values of the daily frequency IPC time series and a combination of several atmospheric and ocean surface variables, a composite analysis will be applied to search for such patterns related to the interannual variability of the IPC. This analysis will not limit the analysis to simple indices that do not enclose the complex variability of several variables at a time over the study area.

The extremes of daily time series of the IPC occurrence have already been used to infer the water mass characteristics related to these extremes. The same P80 and P20 day sets will also be used to identify the atmospheric circulation anomaly patterns that occur prior to the strongest anomalies of occurrences and non-occurrences of the

OSD
9, 3795–3850, 2012

IPC. Assuming that time lagged relations may well occur, lagged versions of P80 and P20 are created by displacing the dates a given lag consequently. Accordingly, two composite patterns for each variable will be computed by averaging the spatial fields of the variable over the dates with extreme IPC, one for the positive (related to P80) and another for the negative (related to P20) cases. Then the negative composite is subtracted to the positive one ($C_{P-N} = C_P - C_N$), and finally, a t-test of significance of this difference is performed at every grid cell and values are only shown on locations where the null hypothesis of equal means is rejected at the 95 % confidence level.

This methodology was applied to eight variables whose characteristics and spatial coverage were described in Sect. 2.1: the 500 hPa level geopotential height anomalies from the ERAInterim reanalysis and the approximated location of the storm track estimated from filtered geopotential height anomalies; the anomalies of the surface pressure; the surface turbulent fluxes; the surface wind stress taken from the reanalysis; the curl of those wind stress anomalies and the sea level anomalies and related geostrophic current anomalies obtained from AVISO. The time spans for the ERAInterim and AVISO variables are 1981–2010 and 1992–2010, respectively. Figure 10 shows the resulting C_{P-N} patterns, displaying pixels in which the differences in the mean were statistically significant (white pixels and missing arrows or contours where not). The first and second columns show the results for the 0–15 and 15–30 day lag spans, respectively. Identical results were also obtained for the 30–45, 45–60, 60–75, and 75–90 day lag spans. The first row (Z) displays the difference patterns C_{P-N} for the 500 hPa height anomalies (black contours) and the red and blue contours represent the C_P and C_N, respectively. The approximated location of the storm track is represented by the colour scale. The second row (SURFACE) shows the patterns for the surface pressure (white contours), wind stress (arrows) and turbulent fluxes (color scale) together, and the third row (SLA) those for the sea level anomaly. Finally, the last row shows the results for both the sea level anomaly (color scale) and geostrophic current anomaly patterns (arrows), and also those of the wind stress curl (blue contours for positive values and white ones for negatives), for the Bay of Biscay area.

OSD
9, 3795–3850, 2012

The composite results for the atmospheric 500 hPa level in the first row of Fig. 10 show that there are distinct circulation schemes associated with the positive and negative composites, observable both in the location of the storm track and the 500 hPa heights. The location of the storm track, for both the 0–15 and 15–30 day lag ranges, is shifted west-southward in the case of C_P with respect to C_N, as evidenced by the positive and negative values in those areas (color scale). The red isolines displaying 500 hPa height composite for the P80 set are shifted southward with respect to the P20 composite, with the exception of the easternmost area where the opposite is observed. Those displacements are summarised by the west-east dipole in the difference pattern (black). As the time lag grows in time, the difference pattern of the storm track location is slightly reinforced and the positive difference area of the 500 hPa height is also slightly shifted northward. The results for the 30–45, 45–60, 60–75, and 75–90 day lag ranges (not shown) indicated a progressive reinforcement of the south-west positive value area (maximum for 45–60 day lag range) coincident with a progressive weakening of the negative value areas. This possibly indicates a faster weakening of the P20 pattern compared to the P80 pattern. However, significant differences are observed for most of the locations up to the 75–90 day lags. Meanwhile, the differences in the 500 hPa heights are less persistent and shrink faster with increasing lags.

The composite patterns (C_{P-N}) of the anomalies of pressure, turbulent flux and wind stress from ERAInterim, in the second row, show mutually coherent patterns. The low pressure anomaly area is centred around 25° N–50° N, the wind patterns are coherent with the pressure patterns under the geostrophic approximation. The negative and positive anomalies of the turbulent flux are located in the west/south-west and east/north-east sectors of the pressure anomaly, respectively, where advection from more northerly or southerly locations occurs (Zorita et al., 1992). Note that the surface centre of action is slightly shifted to the north-east with respect to the 500 hPa pattern. At the surface, the pattern is also persistent for growing lags, with a progressive but slight weakening, and with statistically significant values up to the 60–75 day lag range.

OSD
9, 3795–3850, 2012

SLA maps in the third row show a structure co-located and spatially coherent with that of the heat fluxes in the previous row. Negative anomalies are located in the west/south-west sector and positive anomalies in the eastern/north-eastern. This pattern is noisy in the area of the Gulf Stream, and also to a lesser extent in the rest of the area in relation to the eddy signal. The overall SLP pattern points to an anti-clockwise circulation anomaly, resulting in a weakening of the predominant anticyclonic circulation, i.e. a weakened North Atlantic Gyre. Positive anomalies are located near the coast in the eastern Atlantic boundary over the continental shelf, especially from the western Iberian coast to well to the north of the British isles, indicating the presence of poleward flowing geostrophic currents along most of the eastern Atlantic boundary. In fact, both the SLA and the related geostrophic currents are shown in the last row of Fig. 10, for the Bay of Biscay area. Close to the Iberian coast the currents follow the continental slope (200 m depth black contour), flowing northwards along the the western coast, changing direction at the north-western Iberian corner and then turning eastward with an apparent weakening, in the Cabo Peñas area. Further north, close to the French continental platform the geostrophic currents also seem to follow the continental slope up to approximately 47° N, drifting to the shallower waters near the coast of Brittany coast first and then northwards. With increasing time lags, the altimetry composite shows a persistent behavior maintaining significant values up to the 75–90 day lag range, like in the case of the previous variables. Although the weakening of the pattern is faster close to the Iberian coast, it declines slowly when the whole area is considered.

Additionally, two variables that have been described to modulate the development of IPC events were also considered: the positive wind stress curl, which is related to the related planetary and topographic β effects, and the JEBAR effect, related to the poleward decline of steric sea level. The JEBAR effect is expected to develop at the western Iberian coast, but not at the northern coast, due to the relative orientations of the steric sea level gradient and the coast (Pingree and Le Cann, 1990). Such gradient was accordingly computed between two 1° latitudinal bands of 2° longitude width (14–12° W) centred at 40° N and 43° N using the Absolute Dynamic Topography obtained

OSD
9, 3795–3850, 2012

from AVISO. The P80 composites (C_P) of the gradient for the 0–15 and 15–30 day lag show $\sim 2 \times 10^{-8}$ and $\sim 1 \times 10^{-8}$ values, while the rest of the positive lags yield approximately null values, indicating JEBAR favorable conditions in the western Iberian coast in the month previous to the major IPC events. With regards to the β effect, Le Cann and Serpette (2009) showed (Fig. 9) that the climatological wind stress curl was positive in the western Iberian coast, negative in western part of the northern coast and positive again in the eastern part, favoring the poleward flow in locations where it was positive. The winter climatological mean of the ERAInterim wind stress showed a very similar spatial distribution (not shown). In addition to the climatological mean, the C_{P-N} composite of the anomalies of the wind stress curl was also computed. The corresponding contours are shown in the last row of Fig. 10, where significant positive and negative anomalies are denoted by blue and white contours respectively. The significant values near the coast form a pattern that is similar to that of the winter climatology, indicating a reinforcement of the long-term mean pattern in the P80 set.

A final set of composite patterns was derived to find out if the full set of coherent relations based on the local SST of the Bay of Biscay and shown in the Fig. 10, also had a counterpart in the SST signal of the whole North Atlantic sector. For this purpose the AVHRR Pathfinder V5.2 data (quality flag 7 unreconstructed) was retrieved for those days belonging to P80 and P20 sets. To observe both the developing and decaying phases of the process, negative lags (days after a major IPC event) were also taken into account. Figure 11 shows the (C_{P-N}) patterns for the −15–0, 0–15 and 15–30 day lag ranges. The SST patterns show an intensification and then a decay of the SST signal in the eastern sector. The overall pattern is very consistent with those of the SLA and the surface turbulent fluxes.

4 Discussion

The first part of this study, devoted to the reconstruction of gappy SST data using the DINEOF technique and the verification of such reconstructions, is of crucial importance

OSD
9, 3795–3850, 2012

for the analysis on the IPC carried in the second and third parts, but it is also a valuable scientific result on its own. Although the percentages of missing data were initially very high (up to 93 %), it was possible to reconstruct between 35 % and 45 % of the total days, depending on the reconstruction, with acceptable verification index values, as shown in Table 1. A similar reconstruction based on the 1985–2009 Pathfinder v5.0 data can be found in Esnaola et al. (2012), but for the whole year in that case. The percentage of reconstructed days was higher (above 50 %) as data for the entire year were considered and the verification indices were also slightly better due to the same reason. A comparison of their results with the results shown in the Table 1 indicates that for the full reconstructed set a BIAS of −0.18 °C and a MAD of 0.42 °C were obtained against the −0.31 °C and 0.46 °C analogues derived here. It has to be stressed that in Esnaola et al. (2012) the background error given by the comparison of in situ ICOADS data and the originally non-missing satellite data was also lower (−0.12 °C and 0.35 °C BIAS and MAD values compared to our −0.19 °C and 0.47 °C ones). Consequently, the quality of the reconstruction can be considered in the range of the previous reconstructions for this area. Additional confirmation of the quality of the reconstructions was also provided by the spatial error maps given in Fig. 2 and by the time evolutions of the error displayed in Fig. 3.

The joint use of infra-red and micro-wave SST images in the framework of the DINEOF reconstruction technique is a novel approach that was applied in this study for the Bay of Biscay area. Previous multi-variable approaches have been developed in the context of DINEOF (Alvera-Azcárate et al., 2007), but not for the combination used in this study, that had only been applied in the two-dimensional variational data assimilation (2DVAR) context (Chao et al., 2009). This combination allowed the reconstruction of an additional 4 % of the days without any impact on the verification skill indices (Table 1). In the second and third parts of the present study, where the analysis was focused on the IPC, this combined reconstruction lost prominence in favor of the considerably longer 1981–2010 reconstruction. It has to be pointed out, however, that the IPC evolution time series obtained from this reconstruction (Fig. 7, blue points) show

OSD
9, 3795–3850, 2012

a good agreement with the one derived from the longer time series. Consequently, this combined infra-red and micro-wave SST reconstruction approach has shown to be a valuable methodological improvement that will gain potential as the micro-wave image series become longer. Additional combined approaches, such as combining SST data with altimetry, or other satellite-derived surface products could prove to be valuable for studies related to the IPC and the winter-time SST variability in the Bay of Biscay area.

Once the SST reconstructions were computed and verified, a PCA analysis was applied to isolate the main variability mode. This mode was then subjected to an exhaustive comparison with previous works on the IPC. The shape of the related spatial pattern showed the strongest anomalies near the western Iberian coast, then weakened in the central part of the northern coast to be reinforced again by the east of the Bay and to the north. This shape could be well related to the shape of the climatological mean of the wind stress curl (Le Cann and Serpette, 2009), to its composite anomaly pattern shown in Fig. 10, and to the shape and narrowness of the continental shelf together with the instability of the flow over this area.

The comparison of individual IPC detections based on SST images in previous studies (Table 2) showed a clear agreement with our estimations of the interannual variability of the IPC shown in Fig. 7. For some studies focused only on the western Iberian area (Peliz et al., 2003, 2005), or the IPC time series estimations related to this area (Peliz et al., 2005; deCastro et al., 2011), the agreement was found to be worse. This can be explained by the fact that our EOF analysis points to well developed IPC events (those entering the inner Bay, or Navidad events), which do not have to necessarily match all events at the western coast. Relative to the IPC event occurrence and strength described in Garcia-Soto (2004), the main disagreement is found for the 2001/2002 winter, where the number of reconstructed days is small, and thus our series is not giving much information. Another winter that should be considered with care is 1998/1999 as the signal is very noisy compared to the rest.

OSD
9, 3795–3850, 2012

Differences were also found between our IPC series and the estimation by Le Hénaff et al. (2011). This is not surprising, however, as discrepancies also occur between their two estimated series, and also because there are large methodological differences with our analysis. Their methodology was focused on a single satellite track where the geostrophic current anomalies where deduced. Conversely, our study is focused on a large area. Additionally, the SST anomaly was also computed across the same track as the difference between SST in the areas expected to be affected by the current (between 200 m and 1500 m isobaths) and SST in open-ocean areas, but this was done based on a very small number of satellite SST estimations. The methodology proposed by these authors is promising but suffers from the limited availability of SST data. In fact, this problem can be by-passed using a data reconstruction strategy like the one presented here. The results from such a combination would then be comparable to the estimation of the IPC from a PCA analysis. More general combinations of SST and geostrophic current anomaly data could also be explored to target a joint detection of the IPC signal, e.g. in the form of a Combined PCA or a Canonical Correlation Analysis (Wilks, 2006).

The November to February period used in this study has shown to be a good time framework to study the variability of the IPC in the context of a PCA analysis. However, in some of the strongest IPC developments shown in Fig. 7 (1997/1998, 2002/2003, 2005/2006, 2006/2007) it fails to capture the onset phase of the process, which seems to have occurred during October or earlier. The role of an early IPC development on its subsequent strength is a subject that should be addressed by future studies. However, the results shown here point that in some cases a thorough study of events developed during October would be interesting. Nevertheless, the inclusion of all October months could potentially affect the results of the EOF analysis. This is, therefore, an interesting point for future studies.

The exhaustive checking and comparisons with previous studies have shown a very high level of coherence in most of the cases, confirming our hypothesis that the

OSD
9, 3795–3850, 2012

interannual variability of the surface signal of the IPC can be characterized by the series in Fig. 7.

The combination of results in Fig. 9 for areas I and IV is very consistent with the water mass analysis of cruise data (October–November 1999) carried out by Torres and Barton (2006) for the onset and preliminary development stages of the IPC on the western Iberian coast. Related to the decadal changes in the ventilation conditions of the $ENAW_P$, especially due to strong winter mixing, Pérez et al. (1995) and Pollard et al. (1996) found a shift in water characteristics towards more saline or colder waters relative to the ENAW definition. This is not the case, or at least it is not clear, for the T/S diagrams in Fig. 9, where such decadal variability may have been blurred due to the inclusion of data from 3 different decades.

A subsurface salinity maximum located near the slope has already been identified as a tracer of the poleward flow near the Iberian coast (Frouin et al., 1990; Torres and Barton, 2006). For well developed IPC conditions, Torres and Barton (2006) found this maximum to be well defined by both the northern and western Iberian coasts. Results for the areas I and II in Figs. 8 and 9 show that the salinity maximum is detected in both cases. Le Cann and Serpette (2009) showed that the sub-surface salinity maximum both weakens and looses seaward extension from the slope as the current moves eastward along the northern Iberian coast. This can explain the fact that it was not detected in area III. The presence of the sub-surface salinity maximum and the coherence of the results shown here with those from previous studies are additional support for the validity of the time series given in Fig. 7.

It is interesting to point out that almost all the values related to the western Iberian coast P20 (area I) lay below the ENAW definition line and that the related P20 mean vertical temperature and salinity profiles (Fig. 8) showed colder but saltier waters. The T/S diagram for area IV does not show analogously enhanced salinity values. This rules out a southward advection, but it does show slightly higher salinity in the upper meters (Fig. 8). This result could indicate that a local salinification takes place in winter

OSD
9, 3795–3850, 2012

near the western Iberian coast in strong non-IPC years. It may be due to enhanced evaporation combined with vertical mixing, as suggested by Fig. 10.

In summary, the analysis of the properties of the water masses in winters with extreme values of the IPC series has provided additional confirmation of our working hypothesis.

Once it was well established that the interannual variability of the IPC can be characterized by the series in Fig. 7, a composite analysis was carried out to try to find relations with variables that could have some influence forcing such variability. This composite analysis, summarised in Figs. 10 and 11, revealed a very coherent scenario between the surface atmospheric variables, ocean surface altimetry and temperature characteristics, and also the atmospheric 500 hPa level atmospheric circulation anomalies. These act jointly to create the conditions that favor the development of IPC events. In addition, this set of composite patterns is able to confirm the presence of several mechanisms that had been separately proposed to be related to the variability of the IPC. Our analysis suggests that a combined physical mechanism emerges as discussed below.

Figure 10 shows that a circulation anomaly emerges on the 500 hPa level with an associated anomaly on the approximated location of the North Atlantic storm track. The IPC time series used to deduce this circulation pattern shows a complex relationship with the most common Northern Hemisphere teleconnection patterns, as was shown in Sect. 3.3. Related to the 500 hPa circulation anomaly; pressure, heat-flux and wind-stress anomalies are observed on the surface level. The surface pressure and wind-stress anomalies show anomalous south-westerlies over the Bay of Biscay area. This result is in agreement with many previous studies (e.g. Frouin et al., 1990; Torres et al., 2003; deCastro et al., 2011) that related the IPC occurrences to southerly or south-westerly wind anomalies. In addition to the surface wind anomalies, the surface heat-flux anomalies were also considered here in the context of the IPC. The heat-flux anomaly patterns shown in Fig. 10 are the consequence of the meridional anomalous advection induced by the already mentioned surface pressure and wind stress

OSD
9, 3795–3850, 2012

anomalies. Accordingly, the surface heat-flux anomalies are negative in the west and positive in the east, indicating an anomalous loss and gain of energy by the ocean, correspondingly. Meanwhile, the surface heat-flux anomalies also show a very good correspondence with the SLA patterns. Those show a west/east dipole structure that indicates an anomalous anti-clockwise geostrophic circulation, with a poleward flow on the eastern North Atlantic. These large scale patterns also have a gradient of steric sea level associated on the western Iberian coast, indicating JEBAR favorable conditions over that area (Huthnance, 1984, 1995; Torres and Barton, 2006). Finally, this western Iberian area seems to be also related to positive wind-stress curl anomalies that would reinforce the already positive climatological (Le Cann and Serpette, 2009) mean and favor the poleward flow due to the topographic β effect.

Garcia-Soto et al. (2002) and Garcia-Soto and Pingree (2012) suggest that the poleward current over the eastern North Atlantic slopes could develop in unison. They call this the European Poleward Current, whose Iberian margin branch would be the IPC. Figure 11 shows the SST anomaly patterns related to the patterns shown in Fig. 10. These patterns are in very good agreement with the surface atmospheric anomaly patterns and the SLA patterns. Over the eastern North Atlantic slopes north of the Iberian Peninsula, the evolution of SST anomalies suggests some evidence of the European Poleward Current. However, further research is needed to check the validity of this hypothesis.

The analysis of the patterns shown in Fig. 10 and their analogues with lags going longer back in time, indicated strong persistence properties for the atmospheric variables and slightly weaker persistence properties for the SLA patterns. This was also the case for the gradient of steric sea level by the western Iberian coast. In the case of the SST anomalies over the Iberian shelf and slope (Fig. 11), the evolution phase seems to develop mostly in the 0–15 day range. The time interval of the decay also seems to be in the same range. This would indicate that the atmospheric anomaly patterns need to be persistent enough (up to 60–90 days) to force the oceanic conditions that favor the development of the IPC. In this context the poleward current could be understood

OSD
9, 3795–3850, 2012

as a transient response to a persistent enough atmospheric forcing. Accordingly, the time persistence properties of the anomalies of the oceanic variables are those of the IPC itself.

The cause of the altimetry anomalies observed in the third row of Fig. 10 could be attributed to the action of the surface turbulent fluxes and the surface wind stress shown in the second row of the same figure, or to both. In the case of the surface turbulent heat fluxes, the positive altimetry anomaly would be caused by the steric expansion resulting from the anomalous gain of heat. The Ekman transport related to the wind stress patterns could also be responsible for the observed altimetry anomalies. The good resemblance of the geostrophic current patterns shown in Fig. 10 with the current pattern obtained by Pingree and Le Cann (1989) for constant south-westerly winds (like the ones shown in Fig. 10), also points to that conclusion. The eastern North Atlantic sea level variability at decadal scales was found to be related to the variability of the alongshore wind component and the heat-fluxes by Calafat et al. (2012). They concluded that, for such decadal scales, the influence of the alongshore wind component dominates over the influence of heat fluxes. It is not clear, however, if that is the case for the shorter time-scale altimetry and geostrophic current anomalies studied here, so future studies should deal with the determination of the relative strengths of the heat-flux and wind stress anomalies. It is worth mentioning, that such future studies should also determine if the eddy-like structures observed in the current anomaly patterns, especially those north of the Iberian coast, are physically meaningful or just an artifact of the composite analysis.

A relation of a weakened North Atlantic Gyre and the development of the IPC was first pointed by Pingree (2002). Later, Garcia-Soto and Pingree (2012) showed the changes in the long-term NAO conditions from high (1993–1995) to low (1995–1997) values, and the ensuing changes in the SLA and SST patterns, associated with a weakening of the North Atlantic Gyre. Their SLA and SST anomaly patterns, differences between 1995 and 1998 January means, are very consistent with our slightly weaker patterns in Figs. 10 and 11. It should be noted that despite the good resemblance,

OSD
9, 3795–3850, 2012

some caution is needed. Their analysis was based on a particular period and attributed the differences to long term integrated response of the ocean to dominating positive or negative NAO phases in previous years. Conversely, our results are based on a longer analysis-period and suggest a shorter response time scales. This does not necessarily mean that the two results exclude each other, as the mechanism of integrated anomalies proposed by Garcia-Soto and Pingree (2012) could be conditioning the selection of the P80 and P20 sets. The determination of the relative role of these long term modulations on the shorter time scales, that have been shown to be statistically significant in this study, will be an encouraging challenge for future studies.

5 Conclusions

Winter-time DINEOF reconstructions of the Pathfinder v5.2 1981–2010 SST data and the combined 2002–2010 Pathfinder v5.2 and AMSR-E SST data were validated using in situ data. Similar verification indices were deduced for both the combined and non-combined DINEOF reconstructions. This means that, when available, micro-wave SST images could be used as a complementary source of information when reconstructing infra-red SST images, allowing a major percentage of SST images to be reconstructed.

The IPC was found to be well characterized by the first mode of a PCA analysis conducted on the reconstructed 1981–2010 Pathfinder v5.2 SST data and the 2002–2010 combined Pathfinder v5.2 and AMSR-E SST data. The first EOF showed the spatial structure expected for the SST anomalies related to the IPC. The associated PC or time series that characterizes the variability of the IPC during the winters in the 1981–2010 period was exhaustively compared with results from previous studies that are sumarised in Table 2 to conclude a very good agreement in general. The vertical temperature and salinity distributions related to the extremes of that time series also confirmed its validity. In consequence, the time series shown in Fig. 7 was found to reasonably well characterize the winter-time evolution of the IPC in the 1981–2010 period.

OSD
9, 3795–3850, 2012

A physical mechanism that jointly takes into account both the atmosphere and the ocean was presented in relation to the variability of the IPC. Previous studies had related the variability of the IPC to the occurrence of south-westerly winds, to the JEBAR effect, to the topographic β effect, to a weakened North Atlantic Gyre and also to different North Atlantic atmospheric teleconnection patterns. The joint physical mechanism presented here shows a mutually coherent set of patterns of SST, SLA and ocean surface atmospheric pressure, wind-stress and heat-flux over the North Atlantic that possibly have their origin in a 500 hPa circulation anomaly. The IPC time series used to deduce this circulation anomaly pattern does not show a preferred relation with any of the most common North Atlantic teleconnection patterns. Related to these North Atlantic scale patterns, conditions for a weakened North Atlantic Gyre were obtained. In addition, local characteristics of these patterns indicate south-westerly winds and JEBAR and topographic β effect favorable conditions over the Bay of Biscay area.

Acknowledgements. ERA-Interim data were obtained from the ECMWF data server (http://data.ecmwf.int/data). Pathfinder V5.2 data were provided by GHRSST and the US National Oceanographic Data Center. AMSR-E data are produced by Remote Sensing Systems and sponsored by the NASA Earth Science MEaSUREs DISCOVER Project and the AMSR-E Science Team. Data are available at www.remss.com. The altimeter products were produced by Ssalto/Duacs and distributed by Aviso, with support from Cnes (http://www.aviso.oceanobs.com/duacs/). ICOADS data for this study have been retrieved from the Research Data Archive (RDA) which is maintained by the Computational and Information Systems Laboratory (CISL) at the National Center for Atmospheric Research (NCAR). Word Ocean Database data were obtained from http://www.nodc.noaa.gov/OC5/WOD/pr_wod.html. DINEOF source code is freely available in http://modb.oce.ulg.ac.be/mediawiki/index.php/DINEOF. G. Esnaola is supported by a research grant ("Interacción Atmósfera-Océano en el Golfo de Bizkaia") from Fundación Centros Tecnológicos Iñaki Goenaga. Jon Saenz would like to thank financial support from projects CGL2008-03321 (Spanish National R+D+I Programme) and CTP1O-03 PYNATEO (Basque Government). He also thanks funding provided by the University of the Basque Country (UFI 11/55 and GIU 11/01). The authors want to express their gratitude to A. Caballero from AZTI-Tecnalia for her help with the Altimetry data and to B. Le Cann from UBO-CNRS-

OSD
9, 3795–3850, 2012

IRD-IFREMER for his useful comments on an early draft of this document. This is contribution number XYZ of the Marine Research Division of AZTI-Tecnalia.

References

Alvera-Azcárate, A., Barth, A., Rixen, M., and Beckers, J. M.: Reconstruction of incomplete oceanographic data sets using empirical orthogonal functions: application to the Adriatic Sea surface temperature, Ocean Model., 9, 325–346, 2005. 3804, 3805

Alvera-Azcárate, A., Barth, A., Beckers, J. M., and Weisberg, R. H.: Multivariate reconstruction of missing data in sea surface temperature, chlorophyll, and wind satellite fields, J. Geophys. Res.-Oceans, 112, C03008, doi:10.1029/2006JC003660, 2007. 3805, 3806, 3824

Alvera-Azcárate, A., Barth, A., Sirjacobs, D., and Beckers, J.-M.: Enhancing temporal correlations in EOF expansions for the reconstruction of missing data using DINEOF, Ocean Sci., 5, 475–485, doi:10.5194/os-5-475-2009, 2009. 3805

AVISO: SSALTO/DUACS User Handbook: (M)SLA and (M)ADT Near-Real Time and Delayed Time Products, SALP-MU-P-EA-21065-CLS, Edition 3.3, available at: http://www.aviso.oceanobs.com/fileadmin/documents/data/tools/hdbk_duacs.pdf, 2012. 3804

Beckers, J. M. and Rixen, M.: EOF calculations and data filling from incomplete oceanographic datasets, J. Atmos. Ocean. Tech., 20, 1839–1856, 2003. 3804

Beckers, J.-M., Barth, A., and Alvera-Azcárate, A.: DINEOF reconstruction of clouded images including error maps – application to the Sea-Surface Temperature around Corsican Island, Ocean Sci., 2, 183–199, doi:10.5194/os-2-183-2006, 2006. 3805

Calafat, F. M., Chambers, D. P., and Tsimplis, M. N.: Mechanisms of decadal sea level variability in the eastern North Atlantic and the Mediterranean Sea, J. Geophys. Res., 117, C09022, doi:10.1029/2012JC008285, 2012. 3830

Casey, K. S., Brandon, T. B., Cornillon, P., and Evans, R.: The past, present and future of the AVHRR Pathfinder SST program, in: Oceanography from Space: Revisited, edited by: Barale, J. G. V. and Alberotanza, L., Springer, 273–288, 2010. 3802

Chao, Y., Li, Z., Farrara, J. D., and Hung, P.: Blending sea surface temperatures from multiple satellites and in situ observations for coastal oceans, J. Atmos. Ocean. Tech., 26, 1415–1426, doi:10.1175/2009JTECHO592.1, 2009. 3824

OSD

9, 3795–3850, 2012

Coelho, H. S., Neves, R. R., Leitao, P. C., Martins, H., and Santos, A. P.: The slope current along the western European margin: a numerical investigation, Bol. Inst. Esp. Oceanogr., 15, 61–72, 1999. 3797
deCastro, M., Gómez-Gesteira, M., Álvarez, I., and Crespo, A. J. C.: Atmospheric modes influence on Iberian Poleward Current variability, Cont. Shelf Res., 31, 425–432, 2011. 3798, 3799, 3810, 3814, 3818, 3825, 3828, 3839
Esnaola, G., Sáenz, J., Zorita, E., Lazure, P., Ganzedo, U., Fontán, A., Ibarra-Berastegi, G., and Ezcurra, A.: Coupled air-sea interaction patterns and surface heat-flux feedback in the Bay of Biscay, J. Geophys. Res.-Oceans, 117, C06030, doi:10.1029/2011JC007692, 2012. 3805, 3824
Frouin, R., Fiuza, A., Ambar, I., and Boyd, T.: Observations of a poleward surface current off the coasts of Portugal and Spain during winter, J. Geophys. Res.-Oceans, 95, 679–691, 1990. 3797, 3798, 3800, 3813, 3827, 3828, 3839
Ganzedo, U., Alvera-Azcárate, A., Esnaola, G., Ezcurra, A., and Sáenz, J.: Reconstruction of sea surface temperature by means of DINEOF: a case study during the fishing season in the Bay of Biscay, Int. J. Remote Sens., 32, 933–950, 2011. 3805
Garcia-Soto, C.: "Prestige" oil spill and Navidad flow, J. Mar. Biol. Assoc. UK, 84, 297–300, 2004. 3798, 3799, 3800, 3813, 3814, 3815, 3818, 3819, 3825, 3839
Garcia-Soto, C. and Pingree, R. D.: Atlantic Multidecadal Oscillation (AMO) and sea surface temperature in the Bay of Biscay and adjacent regions, J. Mar. Biol. Assoc. UK, 92, 213–234, 2012. 3799, 3811, 3813, 3819, 3829, 3830, 3831, 3839
Garcia-Soto, C., Pingree, R. D., and Valdés, L.: Navidad development in the southern Bay of Biscay: climate change and swoddy structure from remote sensing and in situ measurements, J. Geophys. Res.-Oceans, 107, 3118, doi:10.1029/2001JC001012, 2002. 3797, 3798, 3799, 3800, 3811, 3813, 3814, 3818, 3819, 3829, 3839
Gil, J.: Changes in the pattern of water masses resulting from a poleward slope current in the Cantabrian Sea (Bay of Biscay), Estuar. Coast. Shelf S., 57, 1139–1149, 2003. 3797
Haynes, R. and Barton, E.: A poleward flow along the Atlantic coast of the Iberian peninsula, J. Geophys. Res.-Oceans, 95, 11425–11441, 1990. 3797, 3798, 3800, 3813, 3839
Herbert, G., Ayoub, N., Marsaleix, P., and Lyard, F.: Signature of the coastal circulation variability in altimetric data in the southern Bay of Biscay during winter and fall 2004, J. Mar. Syst., 88, 139–158, 2011. 3813, 3839
Huthnance, J.: Slope currents and JEBAR, J. Phys. Oceanogr., 14, 795–810, 1984. 3797, 3829

OSD
9, 3795–3850, 2012

Huthnance, J. M.: Circulation, exchange and water masses at the ocean margin: the role of physical processes at the shelf edge, Prog. Oceanogr., 35, 353–431, 1995. 3829
Johnson, D. R., Boyer, T. P., Garcia, H. E., Locarnini, R. A., Baranova, O. K., and Zweng, M. M.: World Ocean Database 2009 Documentation, NODC Internal Report 20, available at: ftp://ftp.nodc.noaa.gov/pub/WOD09/DOC/wod09readme.pdf, 2009. 3803
Kilpatrick, K. A., Podestá, G. P., and Evans, R.: Overview of the NOAA/NASA advanced very high resolution radiometer Pathfinder algorithm for sea surface temperature and associated matchup database, J. Geophys. Res., 106, 9179–9197, 2001. 3803
Koutsikopoulos, C. and LeCann, B.: Physical processes and hydrological structures related to the Bay of Biscay anchovy, Sci. Mar., 60, 9–19, 1996. 3797
Lau, N.-C.: Variability of the observed midlatitude storm tracks in relation to low-frequency changes in the circulation pattern, J. Atmos. Sci., 45, 2718–2743, doi:10.1175/1520-0469(1988)045<2718:VOTOMS>2.0.CO;2, 1988. 3804
Le Cann, B. and Serpette, A.: Intense warm and saline upper ocean inflow in the southern Bay of Biscay in autumn-winter 2006–2007, Cont. Shelf Res., 29, 1014–1025, 2009. 3797, 3799, 3800, 3811, 3813, 3814, 3815, 3817, 3818, 3823, 3825, 3827, 3829, 3839
Le Hénaff, M., Roblou, L., and Bouffard, J.: Characterizing the Navidad current interannual variability using coastal altimetry, Ocean Dynam., 61, 425–437, 2011. 3799, 3813, 3815, 3818, 3826, 3839
Llope, M., Anadón, R., Viesca, L., Quevedo, M., González-Quirós, R., and Stenseth, N. C.: Hydrography of the southern Bay of Biscay shelf-break region: integrating the multiscale physical variability over the period 1993–2003, J. Geophys. Res.-Oceans, 111, C09021, doi:10.1029/2005JC002963, 2006. 3799, 3815, 3817, 3818, 3839
Michel, S., Treguier, A. M., and Vandermeirsch, F.: Temperature variability in the Bay of Biscay during the past 40 years, from an in situ analysis and a 3D global simulation, Cont. Shelf Res., 29, 1070–1087, 2009. 3799
Peliz, A., Dubert, J., Haidvogel, D. B., and Le Cann, B.: Generation and unstable evolution of a density-driven Eastern Poleward Current: the Iberian Poleward Current, J. Geophys. Res.-Oceans, 108, 3268, doi:10.1029/2002JC001443, 2003. 3814, 3825, 3839
Peliz, A., Dubert, J., Santos, A. M. P., Oliveira, P. B., and Le Cann, B.: Winter upper ocean circulation in the Western Iberian Basin – fronts, eddies and poleward flows: an overview, Deep-Sea Res. Pt. I, 52, 621–646, 2005. 3797, 3798, 3810, 3814, 3816, 3825, 3839

OSD
9, 3795–3850, 2012

Pérez, F. F., Ríos, A. F., King, B. A., and Pollard, R. T.: Decadal changes of the 0–8 relationship of the eastern North Atlantic central water, Deep-Sea Res. Pt. I, 42, 1849–1864, 1995. 3827
Pingree, R.: Flow of surface waters to the west of the British Isles and in the Bay of Biscay, Deep-Sea Res. Pt. II, 40, 369–388, 1993. 3798
Pingree, R.: Ocean structure and climate (Eastern North Atlantic): in situ measurement and remote sensing (altimeter), J. Mar. Biol. Assoc. UK, 82, 681–707, 2002. 3800, 3830
Pingree, R. D. and Le Cann, B.: Celtic and Armorican slope and shelf residual currents, Prog. Oceanogr., 23, 303–338, 1989. 3797, 3830
Pingree, R. D. and Le Cann, B.: Structure, strength and seasonality of the slope currents in the Bay of Biscay region, J. Mar. Biol. Assoc. UK, 70, 857–885, 1990. 3797, 3800, 3813, 3822, 3839
Pingree, R. and Le Cann, B.: Anticyclonic eddy X91 in the southern Bay of Biscay, May 1991 to February 1992, J. Geophys. Res.-Oceans, 97, 14353–14367, 1992a. 3798, 3800, 3813, 3814, 3839
Pingree, R. and Le Cann, B.: Three anticyclonic slope water oceanic EDDIES (SWODDIES) in the Southern Bay of Biscay in 1990, Deep-Sea Res. Pt. I, 39, 1147–1175, 1992b. 3797, 3800, 3811, 3813, 3839
Pollard, R. T., Griffiths, M. J., Cunningham, S. A., Read, J. F., Pérez, F. F., and Ríos, A. F.: Vivaldi 1991-A study of the formation, circulation and ventilation of Eastern North Atlantic Central Water, Prog. Oceanogr., 37, 167–192, 1996. 3827
Relvas, P., Barton, E. D., Dubert, J., Oliveira, P. B., Peliz, A., da Silva, J. C. B., and Santos, A. M. P.: Physical oceanography of the western Iberia ecosystem: latest views and challenges, Prog. Oceanogr., 74, 149–173, 2007. 3797, 3798
Ríos, A., Pérez, F., and Fraga, F.: Water masses in the upper and middle North Atlantic Ocean east of the Azores, Deep-Sea Res. Pt. I, 39, 645–658, 1992. 3817
Rogers, J. C.: North Atlantic storm track variability and its association to the north Atlantic oscillation and climate variability of northern Europe, J. Climate, 10, 1635–1647, 1997. 3804
Sánchez, R. F., Relvas, P., and Delgado, M.: Coupled ocean wind and sea surface temperature patterns off the western Iberian Peninsula, J. Mar. Syst., 68, 103–127, 2007. 3805
Simmons, A., Uppala, S., Dee, S., and Kobayashi, S.: ERA-Interim: New ECMWF reanalysis products from 1989 onwards, ECMWF Newsletter, Winter 2006/7, 25–35, available at: http://www.ecmwf.int/publications/newsletters/pdf/110_rev.pdf, 2007. 3803

OSD
9, 3795–3850, 2012

Torres, R. and Barton, E. D.: Onset and development of the Iberian poleward flow along the Galician coast, Cont. Shelf Res., 26, 1134–1153, 2006. 3800, 3813, 3814, 3815, 3816, 3827, 3829, 3839

Torres, R., Barton, E. D., Miller, P., and Fanjul, E.: Spatial patterns of wind and sea surface temperature in the Galician upwelling region, J. Geophys. Res.-Oceans, 108, 3130, doi:10.1029/2002JC001361, 2003. 3797, 3828

von Storch, H. and Zwiers, F. W.: Statistical Analysis in Climate Research, Cambridge University Press, doi:10.2277/0511037538, 1999. 3804

Wilks, D. S.: Statistical Methods in the Atmospheric Sciences, vol. 59, International Geophysics Series, Academic Press, San Diego, California, doi:10.1002/met.16, 2006. 3804, 3807, 3816, 3826

Woodruff, S. D., Worley, S. J., Lubker, S. J., Ji, Z., Freeman, J. E., Berry, D. I., Brohan, P., Kent, E. C., Reynolds, R. W., Smith, S. R., and Wilkinson, C.: ICOADS Release 2.5: extensions and enhancements to the surface marine meteorological archive, Int. J. Climatol., 31, 951–967, 2011. 3803

Worley, S. J., Woodruff, S. D., Reynolds, R. W., Lubker, S. J., and Lott, N.: ICOADS release 2.1 data and products, Int. J. Climatol., 25, 823–842, 2005. 3803

Zorita, E., Kharin, V., and von Storch, H.: The atmospheric circulation and sea surface temperature in the North Atlantic area in winter: their interaction and relevance for Iberian precipitation, J. Climate, 5, 1097–1108, doi:10.1175/1520-0442(1992)005<1097:TACASS>2.0.CO;2, 1992. 3821

OSD

9, 3795–3850, 2012

Table 1. Verification of the 1981–2010 Pathfinder, 2002–2010 Pathfinder and the 2002–2010 combined Pathfinder/AMSR-E DINEOF reconstructions using ICOADS SST data. In all three cases in situ observations are compared with the originally non-missing satellite values (SATELLITE) and with the fully reconstructed dataset (DINEOF). The number of reconstructed days together with the percentage of the total they represent in brackets, the sample size of each verification sub-sample (*N*), the bias (BIAS) and the median absolute deviation (MAD) are shown.

	1981–2010 Pathfinder		2002–2010 Pathfinder		2002–2010 Pathfinder/AMSR-E	
	SATELLITE	DINEOF	SATELLITE	DINEOF	SATELLITE	DINEOF
Days	1256 (35.5 %)	1256 (35.5 %)	418 (40.9 %)	418 (40.9 %)	460 (45.0 %)	460 (45.0 %)
N	8807	42458	2832	16733	2919	18 336
BIAS (°C)	−0.19	−0.31	−0.18	−0.32	−0.18	−0.31
MAD (°C)	0.47	0.46	0.24	0.27	0.24	0.26

OSD
9, 3795–3850, 2012

Table 2. The references, dates and the employed technique for the documented IPC detections during the last decades. Only detections from the months taken into account in this study are shown (November-December-January-February). A brief description is given whenever the number of dates is very high. Studies that do not take into account the inner part of the Bay of Biscay, i.e. limited to the western or north-western Iberian coasts are identified by the WI acronym. ZG stands for the zonal gradient between the coastal and open ocean SST on the western Iberian coast.

Reference	Dates (DD/MM/YYYY)	Method	Time-evolution
Frouin et al. (1990)	06(30)/11/1983, 04(27)(29)/12/1983, 01/01/1984	Infra-red (ind. images)	*
Pingree and Le Cann (1990)	28/12/1983, 28/12/1989, 01(13)/01/1990	Infra-red (ind. images)	*
Haynes and Barton (1990)	11/01/1988	Infra-red (ind. images)	*
Pingree and Le Cann (1992a)	28/12/1983, 28/12/1989, 31/01/1989	Infra-red (ind. images)	1984–1991 Dec-Jan-Feb monthly
Pingree and Le Cann (1992b)	28/12/1983, 28/12/1989, 04(12)/01/1990	Infra-red (ind. images)	*
Garcia-Soto et al. (2002)	17/01/1979, 17/01/1982, 28/01/1983, 09/01/1986, 11(19)/01/1988, 29/01/1989, 12/01/1990, 12/01/1991, 06/01/1992, 22/01/1993, 18/01/1994, 13/01/1995, 18/01/1996, 08(12)(19)(21)(22)/01/1998	Infra-red (ind. images)	1979–2000 Jan (missing 1980, 1981 and 1985)
Peliz et al. (2003)	28/01/1997, 25/02/1998, 09(16)/01/2002	Infra-red (ind. images) (WI)	*
Garcia-Soto (2004)	26/11/2002, 13/01/2003	Infra-red (ind. images)	1979–2003 Jan
Peliz et al. (2005)	28/01/1997, 09/02/1997, 25/02/1998, 09(16)/01/2002	Infra-red (ind. images) (WI)	WI zonal SST gradient 1985–2001 Jan-Feb
Llope et al. (2006)	T/S profile per winter (Dec, Jan or Feb)	In-Situ (WI)	1992–2003 yearly winter mean
Torres and Barton (2006)	31–06/10–11/1999 and Cruise: 13–7/10–11/1999	Infra-red (weekly) and In-situ	*
Le Cann and Serpette (2009)	29/11/2006, 14/12/2006 and Cruise: 6–11/11/2006	Infra-red (ind. images) and In-situ	1995–2006 yearly
deCastro et al. (2011)	1985–2006 Jan	Infra-red (monthly)	1985–2006 Jan
Herbert et al. (2011)	SST: 20/01/2004, 31/01/2004, 01/02/2004 and Alt.: 12–18/01/2004, 1–7/02/2004, 25–01/10–11/2004	Infra-red and Altimetry	*
Le Hénaff et al. (2011)	1992–2002 Dec/Jan and Jan/Feb SST and Topex/Poseidon track 137	Infra-red and Altimetry	1992–2002 (2 months per winter)
Garcia-Soto and Pingree (2012)	01–31/01/1990, 21/12/2000, 12/01/2001, 13/01/2003, 26/11/2006, 14(28)/12/2006, 09/01/2007, 14/02/2007, 25/12/2009, 03/02/2010	Infra-red (ind. images)	*

OSD
9, 3795–3850, 2012

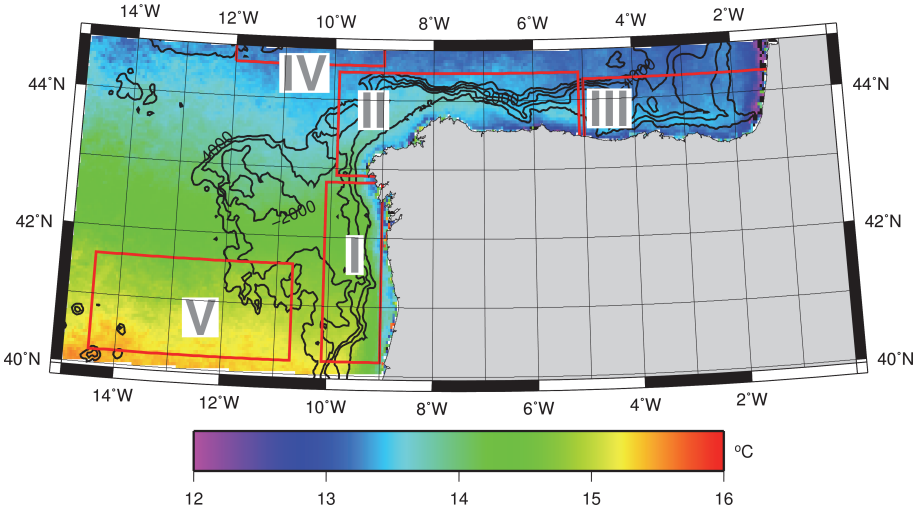

Fig. 1. The main study area with the mean December–January SST distribution. Boxes I to V will be used to create separated vertical temperature and salinity data sets based on the Word Ocean Database individual casts. Area IV (12.0° W–9.0° W 44.5° N–46.5° N) is only partially shown. 1000 m to 4000 m depth contours are shown with a 1000 m depth interval.

OSD
9, 3795–3850, 2012

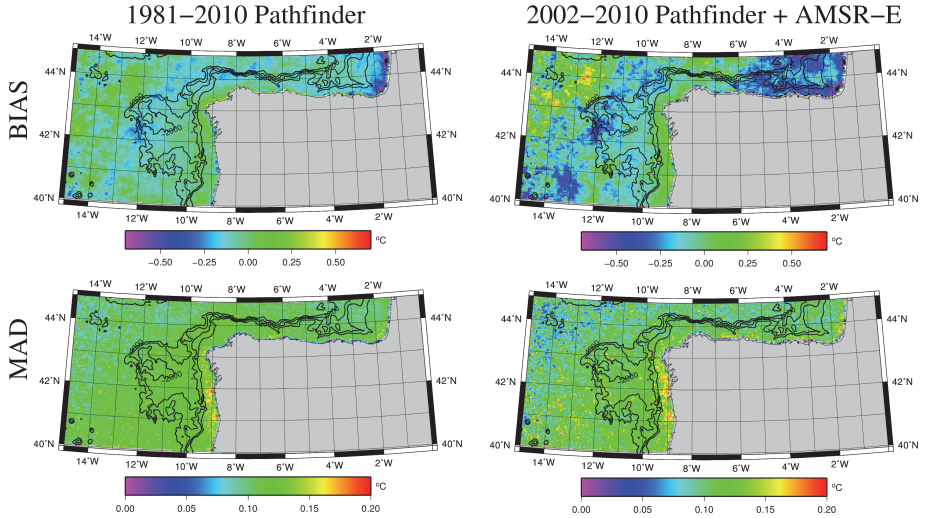

Fig. 2. BIAS (°C, first row) and MAD (°C, second row) error distribution maps obtained comparing originally non-mising satellite data with their reconstructed counterparts. The first column shows error maps for the 1981–2010 Pathfinder alone reconstruction and the second one those of the combined Pathfinder AMSR-E reconstruction.

OSD
9, 3795–3850, 2012

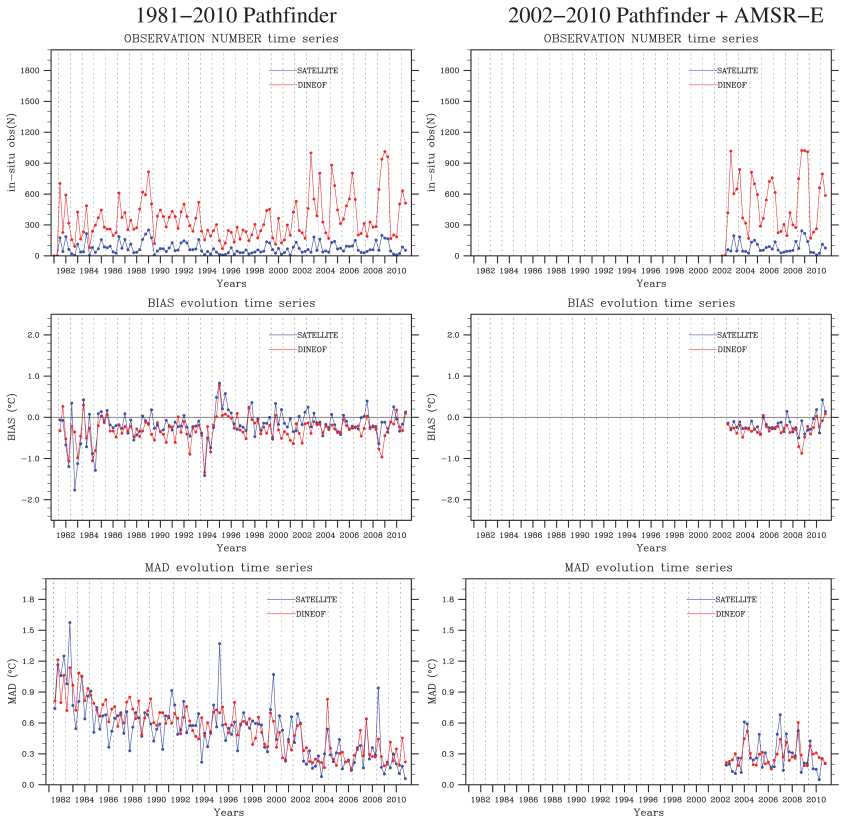

Fig. 3. Time evolution of the monthly Number Of Observations (first row) and the BIAS (second row) and MAD (third row) error estimates. Columns are organized like in Fig. 2. Blue lines indicate estimates obtained from data pairs of originally non-missing satellite data and their ICOADS counterparts while the red ones indicate the same but for the reconstructed datasets. The same time axis is used for the 1981–2010 and the 2002–2010 reconstructions in order to allow an easier comparison.

OSD
9, 3795–3850, 2012

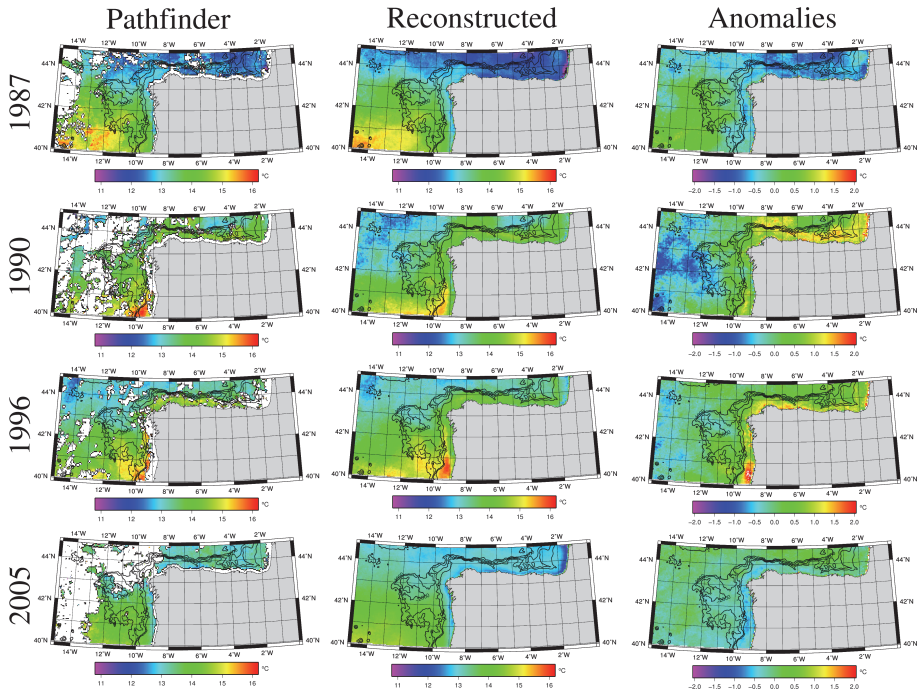

Fig. 4. January SST fields for years 1987, 1990, 1996 and 2005. The first column shows the mean of un-reconstructed flag 7 Pathfinder values of the respective year, the second one the same but reconstructed using DINEOF and the third one also the same but after the climatological mean has been removed.

OSD
9, 3795–3850, 2012

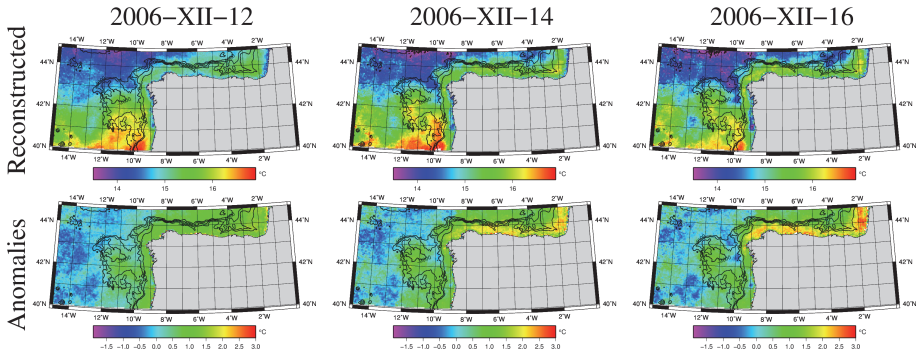

Fig. 5. Reconstructed SST fields (first row) and their related anomalies (second row) for 12th, 14th and 16th January of 2006.

OSD
9, 3795–3850, 2012

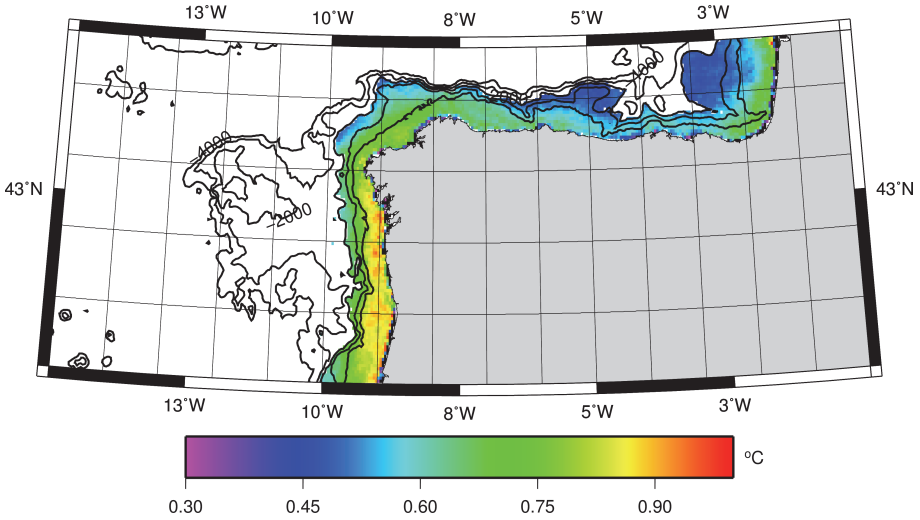

Fig. 6. First EOF of the PCA analysis of the 1981–2010 reconstructed SST dataset when only pixels with a related depth of less than 2000 m are taken into account. The 200 m depth contour is shown in addition to the contour depths shown in previous figures.

OSD
9, 3795–3850, 2012

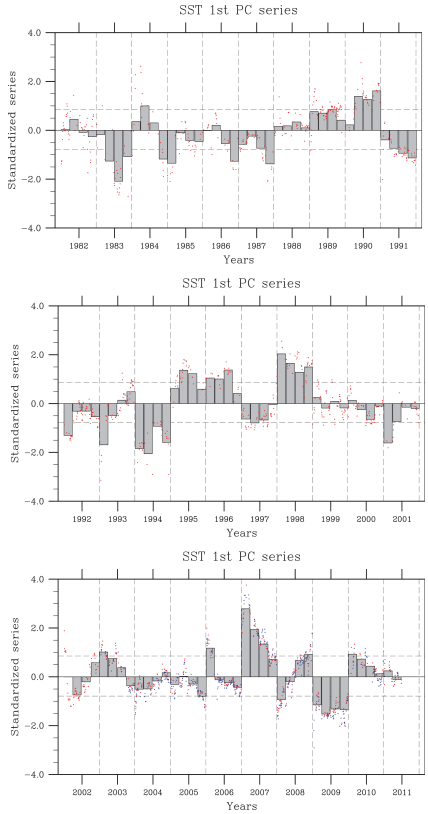

Fig. 7. The PC related to the EOF shown in Fig. 6. Vertical dashed lines indicate jumps from the end of February to the beginning of November of the same year. Red points are related to the PC deduced from the 1981–2010 reconstructed SST PCA analysis and the blue ones to the 2002–2010 reconstruction. Grey vertical bars give the mean monthly values of the red dot values.

OSD
9, 3795–3850, 2012

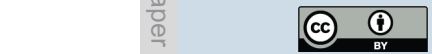

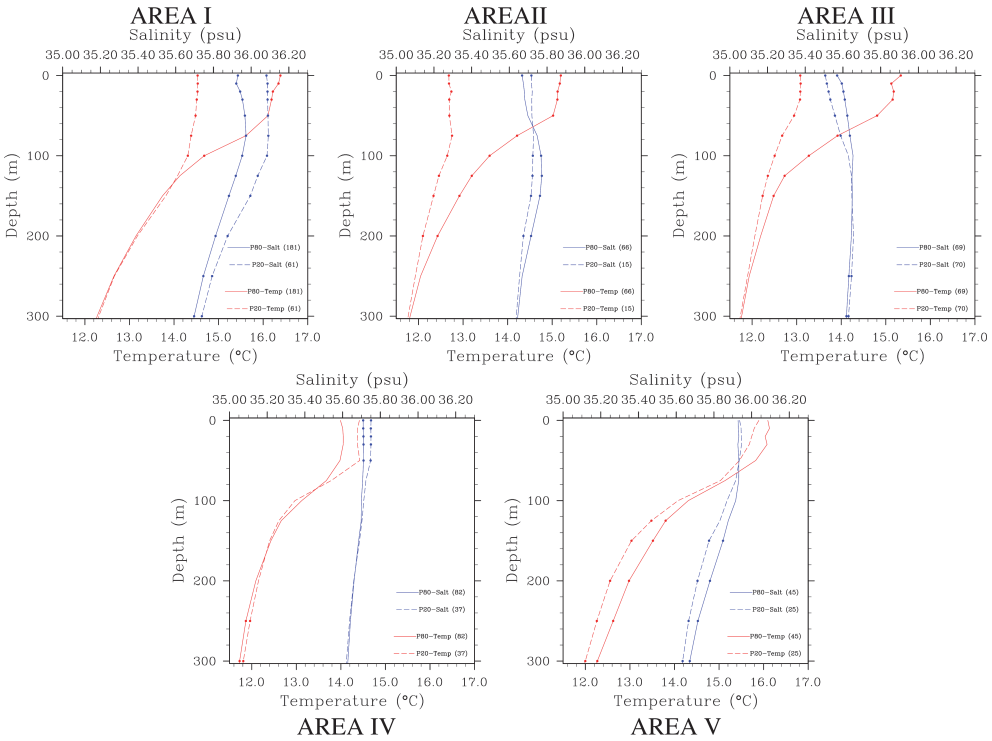

Fig. 8. Mean vertical temperature (red) and salinity (blue) composite profiles related to the P80 (solid lines) and P20 (dashed lines) day sets. Profiles for the ±5 days of each day in the P80 and P20 day sets are taken into account. Each of the 5 figures belongs to the corresponding area shown in Fig. 1.

OSD
9, 3795–3850, 2012

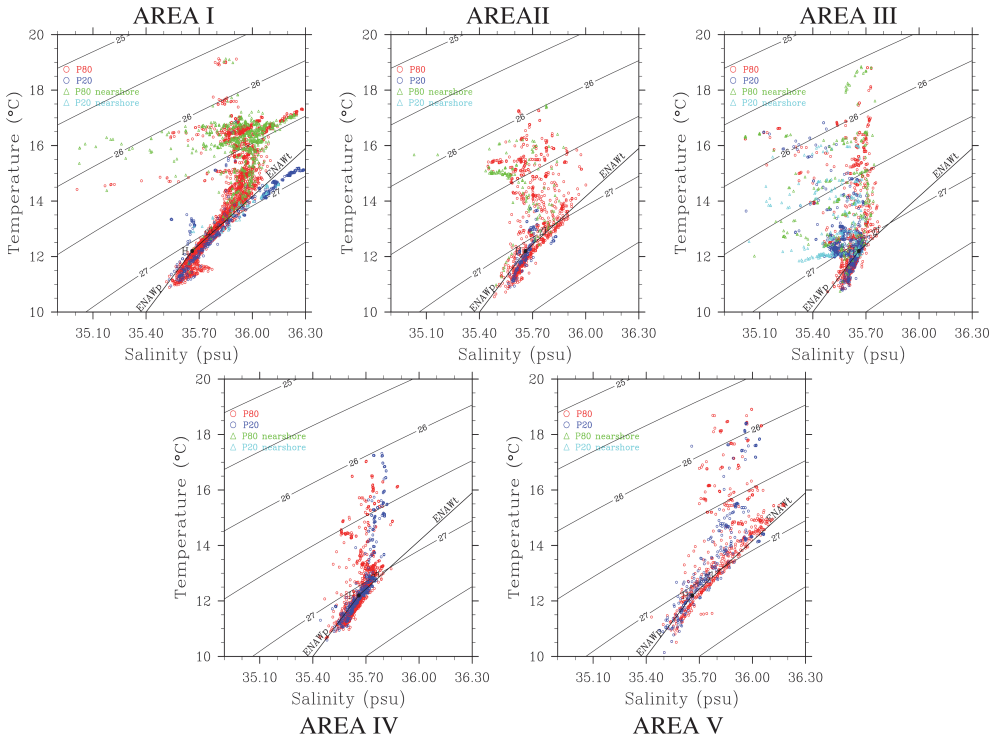

Fig. 9. Like in Fig. 8 but for the T/S diagrams instead of the vertical profiles. The profiles related to shallow (< 200 m, triangles) and deeper waters (circles) are plotted separately, so that the red and green markers are related to the P80 set and the dark and light blue ones to the P20 set.

OSD
9, 3795–3850, 2012

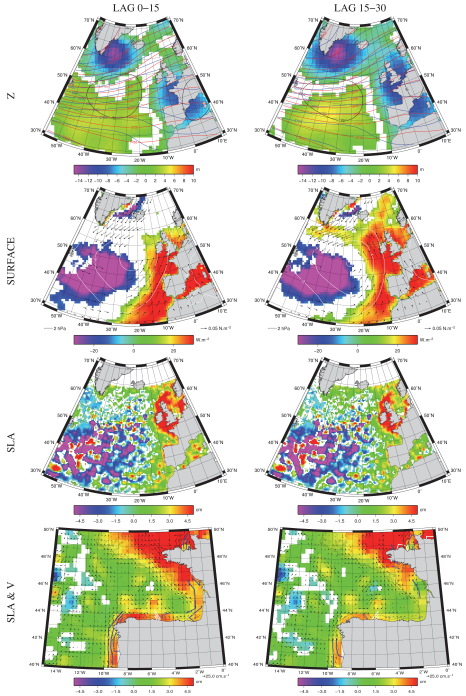

Fig. 10. Composite results based on the IPC time series shown in Fig. 7. The analysed variables are the 500 hPa geopotential height anomalies (first row; red, blue and black contours), the estimated location of the storm track (first row, colour scale), the surface pressure (second row, white contours), the surface turbulent fluxes (second row, colour scale), the wind stress (second row, arrows), the sea level anomalies (third and fourth rows, colour scale) and the related current anomalies (fourth row, arrows) and the curl of the wind stress (fourth row, blue and white contours). 200 m depth contour is shown in the Figures in the last row. The columns correspond to the 0–15 and 15–30 day lag ranges. All variables are masked by the 95 % confidence mask built by means of a *t*-test on the difference of means. See the text for more details.

OSD
9, 3795–3850, 2012

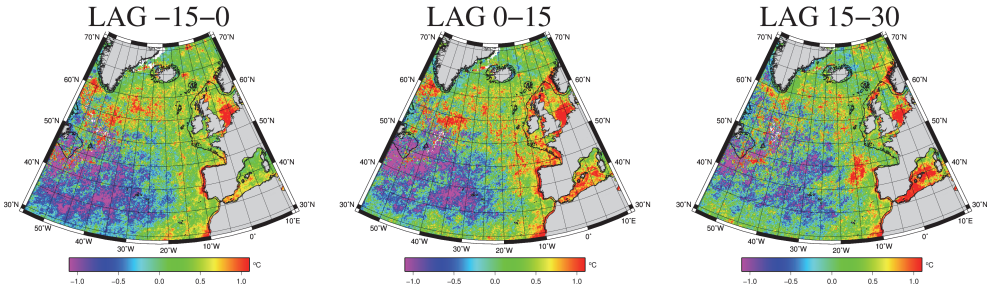

Fig. 11. Similar to Fig. 10 but for the flag 7 un-reconstructed Pathfinder v5.2 data, and also taking into account the −15–0 day lag range.

OSD
9, 3795–3850, 2012